

---

# UNCERTAINTY QUANTIFICATION OF LOCALLY NONLINEAR DYNAMICAL SYSTEMS USING NEURAL NETWORKS

---

A PREPRINT

**Subhayan De**

Aerospace Engineering Sciences  
University of Colorado  
Boulder, CO 80309  
Subhayan.De@colorado.edu

August 12, 2020

## ABSTRACT

Models are often given in terms of differential equations to represent physical systems. In the presence of uncertainty, accurate prediction of the behavior of these systems using the models requires understanding the effect of uncertainty in the response. In uncertainty quantification, statistics such as mean and variance of the response of these physical systems are sought. To estimate these statistics sampling-based methods like Monte Carlo often require many evaluations of the models' governing differential equations for multiple realizations of the uncertainty. However, for large complex engineering systems, these methods become computationally burdensome as the solution of the models' governing differential equations for such systems is expensive. In structural engineering, often an otherwise linear structure contains spatially local nonlinearities with uncertainty present in them. A standard nonlinear solver for them with sampling-based methods for uncertainty quantification incurs significant computational cost for estimating the statistics of the response. To ease this computational burden of uncertainty quantification of large-scale locally nonlinear dynamical systems, a method is proposed herein, which decomposes the response into two parts — response of a nominal linear system and a corrective term. This corrective term is the response from a pseudoforce that contains the nonlinearity and uncertainty information. In this paper, neural network, a recently popular tool for universal function approximation in the scientific machine learning community due to the advancement of computational capability as well as the availability of open-sourced packages like PyTorch and TensorFlow is used to estimate the pseudoforce. Since only the nonlinear and uncertain pseudoforce is modeled using the neural networks the same network can be used to predict a different response of the system and hence no new network is required to train if the statistic of a different response is sought. Three numerical examples are used to show that the proposed method inexpensively produces accurate statistics of the response in the presence of uncertainty.

**Keywords** Uncertainty quantification · nonlinear dynamical systems · neural networks

## 1 Introduction

Models often given by a set of differential equations are used to characterize and express the behavior of a physical system. In these models, the sources of uncertainty can be large, *e.g.*, in material properties, geometry, and loading conditions [1, 2, 3]. An accurate and robust prediction of the behavior of the physical system using these models requires proper understanding of the effects of these multiple sources of uncertainty. Uncertainty quantification using the standard Monte Carlo approach uses many evaluations of the physical system for different realizations of the uncertainty. However, for large and complex structures, this approach soon becomes computationally expensive. Approaches using polynomial chaos expansion [4, 5] and stochastic collocation [6, 7] develop polynomial approximations to reduce the computational burden. However, with increasing dimension of the uncertain variables, the number of terms retained in the expansion increases significantly. Similarly, Gaussian process regression [8] can be used to develop surrogate

models [9] but its training cost increases cubically with the number of data points. The response surface approximations [10, 11] build surrogate models utilizing random samples from the uncertainty but can lead to pitfalls in the presence of a small training sample size [11]. Intelligent sampling techniques (*e.g.*, Latin hypercube sampling [12], stratified sampling [13]) can also be implemented for uncertainty quantification of the response of the physical system for a relatively smaller number of realizations of the uncertainty variables. However, the use of surrogate models with these sampling techniques is straightforward and will provide similar reduction in computational cost for all surrogate modeling techniques.

In structural engineering, an otherwise linear structure often contains spatially local nonlinearities. For example, a building superstructure or a bridge, which behaves linearly under most earthquake or wind excitation, may have a nonlinear base isolation layer [14, 15, 16] or nonlinear tuned-mass damper attached to it [17]. Similarly, spacecrafts often have nonlinear joints [18, 19, 20]. Another example of the presence of local nonlinearity in an otherwise linear structure is contact friction in linear elastic structures [20, 21, 22, 23]. For such large-scale locally nonlinear structures, unless an approximate linearization technique is used the computational cost of using a nonlinear solver for uncertainty quantification becomes unbearable [17]. [24] used an approach for uncertainty quantification of locally nonlinear dynamical systems that solves a nonlinear Volterra integral equation for multiple realizations of the uncertainty. [25, 26, 17, 16] used this approach for Bayesian model selection and design under uncertainty of nonlinear structural systems.

With the availability of highly optimized open-sourced codes like PyTorch [27] and TensorFlow [28] neural networks have found recent popularity in the scientific community [29]. In these Scientific Machine Learning (SciML) applications, neural networks are used for modeling large complex systems for which response prediction is computationally expensive. In [30, 31, 32, 33, 34], the neural networks are trained using a loss function that specifically incorporates the error in the governing differential equations. Using this strategy, the trained networks match the prediction from the governing equations while reducing the computational cost of solving them using methods like finite element. [35] used time-dependent recurrent neural networks to learn turbulence. Generative adversarial networks [36] are used in [37] to generate high-resolution meteorological data from low-resolution images. Neural networks are also used for reduced order modeling in [38, 39]. [40, 41] used neural networks for modeling turbulence by augmenting Reynolds Averaged Navier-Stokes (RANS) models. [42] used neural networks for modeling flow near the wall in Large Eddy Simulation (LES). For estimating structural response, [43, 44] used convolutional and recurrent neural networks. Multifidelity datasets for response of physical systems are used for training neural networks in [45, 46, 47, 48]. Neural networks have also been used for uncertainty quantification of physical systems. For example, [49] and [50] used dropout strategy [51] for quantifying model as well as parametric uncertainty with neural networks, where some of the connections in the networks are ignored with some probability. [52] used convolutional neural networks for developing surrogate models for uncertainty propagation through random field. [53] used neural networks to reduce the uncertainty associated with RANS models. [45] used different transfer learning techniques for uncertainty quantification of physical systems, when training data from an inaccurate coarse model is abundant compared to training data from an accurate fine model. Recently, [54] used this approach of training neural networks for reliability estimation.

In this paper, to reduce the computational burden associated with a nonlinear solver for a locally nonlinear dynamical system under uncertainty the response is decomposed into two parts — a nominal linear response and response from a pseudoforce that takes into account the nonlinearity and any uncertainty. The solution for the pseudoforce, however, leads to a nonlinear Volterra equation of the second kind written in nonstandard form [24]. Hence, to obtain the response for these systems with nonlinearities encountered in structural engineering requires an iterative solver. In this paper, instead, a neural network is trained to accurately predict the pseudoforce. The nominal linear response of the dynamical system is then combined with the pseudoforce response to get an accurate estimate of the total response of the system. Hence, this approach is different than the training method of using physics-informed loss function to satisfy the governing equations. Instead, only a part of the response is modeled in this proposed approach keeping the physics solution for rest of the structure. Further, the same trained network can be used even if the statistics of a different response is sought as these networks model the pseudoforce and not the response directly. Three numerical examples with increasing degrees of freedom (DOF) are used to illustrate the proposed approach. The first example considers uncertainty in a two DOF spring-mass-damper model. The second example uses a 11-story 2-bay 100 DOF building resting on a hysteretic base isolation layer with uncertain properties and subjected to a historic earthquake excitation. A three-dimensional 1623 DOF building with three uncertain tuned mass dampers (TMDs) on its roof is used in the third example. These three numerical examples show that once trained the neural networks used in the proposed approach provide accurate prediction along with large computational gains in uncertainty quantification.

## 2 Background

A brief background on uncertainty quantification using surrogate models is discussed in this section followed by a description of the three different architectures for neural networks used in the numerical examples of this paper. The training of these networks using generated datasets is discussed next.

### 2.1 Uncertainty Quantification

Dynamical systems are often represented by models given by differential equations. In the presence of uncertainty, the system's response  $\mathbf{Y}(t; \boldsymbol{\xi}) \in \mathbb{R}^{n_y}$  depends on the external force  $\mathbf{w}(t) \in \mathbb{R}^{n_w}$  as well as on the random variables  $\boldsymbol{\xi} \in \mathbb{R}^{n_\xi}$  and can be given by

$$\mathbf{Y}(t; \boldsymbol{\xi}) = \mathcal{M}(\mathbf{w}(t), \boldsymbol{\xi}), \quad (1)$$

where  $\mathcal{M} : \mathbb{R}^{n_w} \times \mathbb{R}^{n_\xi} \rightarrow \mathbb{R}^{n_y}$  is the model of the dynamical system. As a result,  $\mathbf{Y}(t; \boldsymbol{\xi})$  is also an uncertain quantity. In this paper, the random variables  $\boldsymbol{\xi}$  are described using known probability distributions. In uncertainty quantification, statistics of the random variables  $\mathbf{Y}(t; \boldsymbol{\xi})$  are sought. The most commonly used approach for estimating such statistics is the Monte Carlo method [55]. For example, the mean and variance of  $\mathbf{Y}(t; \boldsymbol{\xi})$  can be approximated using  $N$  realizations of  $\boldsymbol{\xi}$  as follows

$$\begin{aligned} \mathbb{E}_{\boldsymbol{\xi}}[\mathbf{Y}(t; \boldsymbol{\xi})] &\approx \frac{1}{N} \sum_{i=1}^N \mathbf{Y}(t; \boldsymbol{\xi}_i); \\ \text{Var}_{\boldsymbol{\xi}}[Y_j(t; \boldsymbol{\xi})] &\approx \frac{1}{N-1} \sum_{i=1}^N \left( Y_j(t; \boldsymbol{\xi}_i) - \frac{1}{N} \sum_{k=1}^N Y_j(t; \boldsymbol{\xi}_k) \right)^2; \quad j = 1, \dots, n_y, \end{aligned} \quad (2)$$

where the model  $\mathcal{M}$  may need to be evaluated for  $\{\boldsymbol{\xi}_i\}_{i=1}^N$  for a large  $N$  increasing the computational cost. Surrogate models can be developed in such cases [56], which are computationally inexpensive and can be used in (2). In this paper, neural networks are used to replace some parts of the model  $\mathcal{M}$  while satisfying the governing equations. Note that an intelligent sampling technique can be used instead of (2). However, the focus of this paper is to develop a computationally advantageous strategy for the calculation of  $\mathbf{Y}(t; \boldsymbol{\xi})$ . Same strategy can be applied in conjunction with any other sampling techniques. Hence, the study of different intelligent sampling methods is beyond the scope of this work.

### 2.2 Neural Networks

An artificial neural network, or simply a neural network is widely used for approximating functional relationship such as (1). With recent advancement in the computing power large neural networks are possible to train that can learn the behavior of complex systems. Among many available architectures for the networks the feed-forward, residual, and convolutional neural networks are used in this paper. They are briefly described next.

#### 2.2.1 Feed-forward Neural Network (FNN)

The feed-forward neural network (FNN) or multilayer perceptron (MLP) [57], which consists of an input layer, one or more hidden layers, and an output layer, is commonly used in scientific machine learning applications [29]. Figure 1 shows a schematic of such network, where the network has  $N_H$  number of hidden layers. Each of these hidden layers has  $m$  number of neurons. However, in general, the number of neurons in each layer can be different. Inside each neuron, an affine transformation followed by a nonlinear activation function is applied to the input. Hence, given an input  $\mathbf{v}$  a neural network approximates the output  $\mathbf{z}$  by

$$\begin{aligned} \mathbf{z} &\approx \mathcal{M}_{\text{NN}} \left( \mathbf{v}; \{\mathbf{W}_i\}_{i=0}^{N_H}, \{\mathbf{b}_i\}_{i=0}^{N_H} \right) \\ &= \mathbf{W}_0^T \sigma_{N_H} (\dots (\sigma_1 (\mathbf{W}_1^T \mathbf{x} + \mathbf{b}_1)) \dots) + \mathbf{b}_0, \end{aligned} \quad (3)$$

where  $N_H$  is the number of hidden layers; the weights  $\mathbf{W}_i$  and the biases  $\mathbf{b}_i$  for  $i = 1, \dots, N_H$  are the parameters for the  $i$ th hidden layer that needs to be tuned using the training dataset;  $\mathbf{W}_0$  and  $\mathbf{b}_0$  are the parameters for the output layer; and  $\sigma_i(\cdot)$  is a nonlinear activation function for the  $i$ th hidden layer. There are many choices available for the activation function. For example, the output from a hyperbolic tangent and sigmoid activation functions are, respectively, given by

$$\begin{aligned} \sigma_{\text{tanh}}(z) &= \tanh(z); \\ \sigma_{\text{sigm}}(z) &= \frac{1}{1 + e^{-z}}. \end{aligned} \quad (4)$$

The output from two other popular activation functions, namely, Rectified Linear Unit (ReLU) and Exponential Linear Unit (ELU) are given by

$$\begin{aligned} \sigma_{\text{ReLU}}(z) &= \max(0, z); \\ \sigma_{\text{ELU}}(z) &= \begin{cases} z & \text{for } z > 0, \\ \alpha(e^z - 1) & \text{for } z \leq 0, \end{cases} \end{aligned} \quad (5)$$

where  $\alpha$  is a positive parameter. In this paper, the activation functions are chosen from preliminary runs to produce the smallest validation errors defined in Section 3.2. Figure 2 compares the outputs of these activation functions.

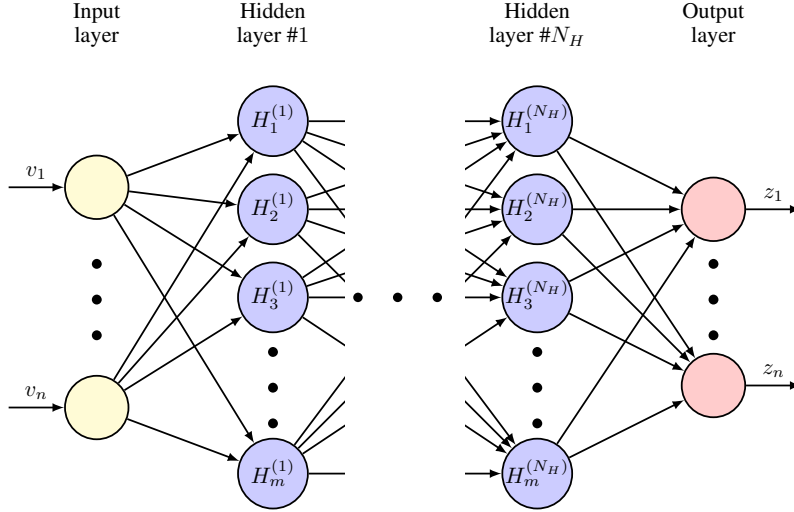


Figure 1: Feed-forward Neural Network (FNN) architecture with  $N_H$  hidden layers. Each of these hidden layers contains  $m$  neurons.

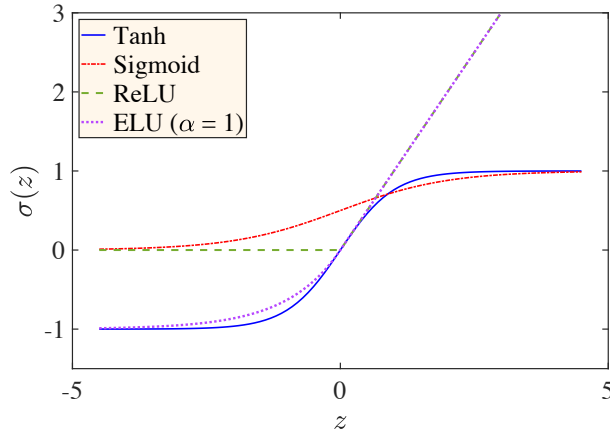


Figure 2: Four different activation functions tested in this paper.

Another popular neural network architecture is tried herein, where the  $i$ th hidden layer models the residual error in the output from the previous layer as shown in Figure 3 with curved arrows. This architecture is known as the residual neural network or ResNet. Hence, the output of a hidden layer that is used to model the residual after  $(i - 1)$ th layer is given by [58]

$$\mathbf{z}_i = \sigma_i(\mathbf{W}_i^T \mathbf{z}_{i-1} + \mathbf{b}_i) + \mathbf{z}_{i-1}. \quad (6)$$

A short-cut mapping [58] must be used if the dimensions of  $\mathbf{z}_i$  and  $\mathbf{z}_{i-1}$  are different.

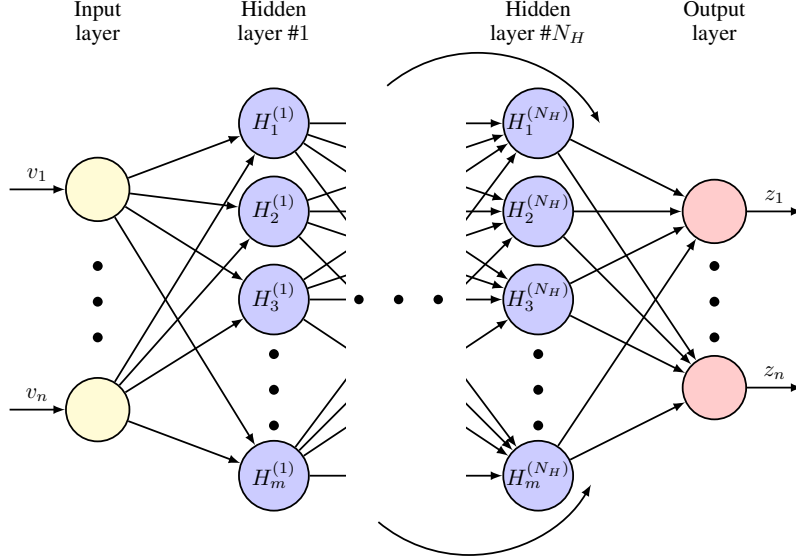


Figure 3: A schematic of the Residual Neural Network (ResNet) with residual connections shown using curved arrows. The network here has  $N_H$  number of hidden layers, where each of these layers has  $m$  neurons.

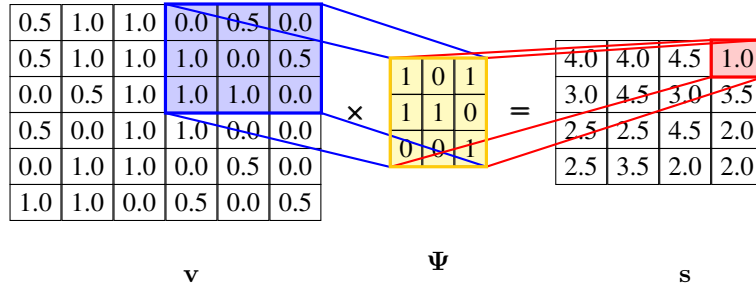


Figure 4: A schematic of the convolution procedure implemented in CNN (see (8)).

### 2.2.2 Convolutional Neural Network (CNN)

The convolutional neural network (CNN) has been developed with inspiration from the vision system at the primary visual cortex of human brain [57]. In CNN, the convolution operation is performed for a two-dimensional input  $\mathbf{v}$  and a kernel  $\Psi$  as follows

$$s_{ij} = \sum_q \sum_r v_{i-q, j-r} \Psi_{qr}, \quad (7)$$

where  $\mathbf{s}$  is the two-dimensional output from a convolutional layer. During training of the CNN, the kernel  $\Psi$  is learned. Note that, zero-padding is required if the output  $\mathbf{s}$  and input  $\mathbf{v}$  are of the same length. Pytorch [27], which is used for the numerical examples herein, however, performs the cross-correlation instead of the convolution given by

$$s_{ij} = \sum_q \sum_r v_{i+q, j+r} \Psi_{qr} \quad (8)$$

for a two-dimensional input  $\mathbf{v}$ , which uses a mirror image of the kernel in (7). Figure 4 illustrates the working of this procedure, where blue shaded elements of  $\mathbf{v}$  are multiplied by  $\Psi$  to get the red shaded element in  $\mathbf{s}$ . A maxpooling operation often follows a convolution operation in which the output from the convolution layer is downsampled using a max function over a window. However, in time histories if the length of both input and output remains same the maxpooling has limited use [43] and can be omitted. These steps inside a single convolutional layer are shown in Figure 5. Note that a kernel with size smaller than the size of the input produces sparse connectivity in the network. This creates a sharing of the parameters and helps in avoiding over-fitting. A typical implementation of the CNN often uses a few convolutional layers followed by feed-forward layers as shown in Figure 6. Note that for  $N$  input of images to the CNN the input has a size  $N \times C \times H \times W$ , where  $C$  is the number of channels (e.g., R-G-B);  $H$  is the height; and  $W$

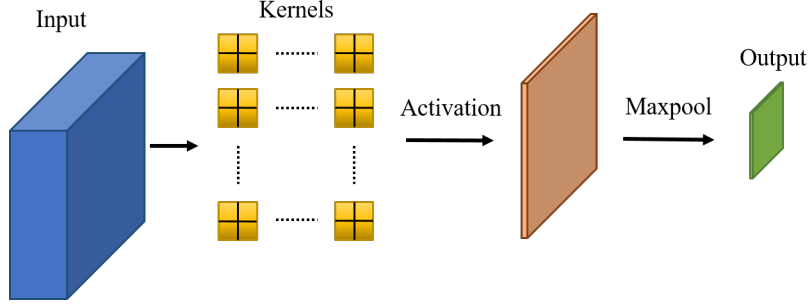


Figure 5: A typical single layer of CNN includes the convolution (see (7)) or cross-correlation operation (see (8)) followed by the activation function and a maxpooling operation.

is the width of the images. For  $N$  input of time-histories, which is used here, the input has a size  $N \times C \times L$ , where  $L$  is the length of time-histories. Here, the response and the uncertain parameters are used as different channels in the input. Further, the number of neurons in the feed-forward layers are assumed to be same as  $L$  in this paper.

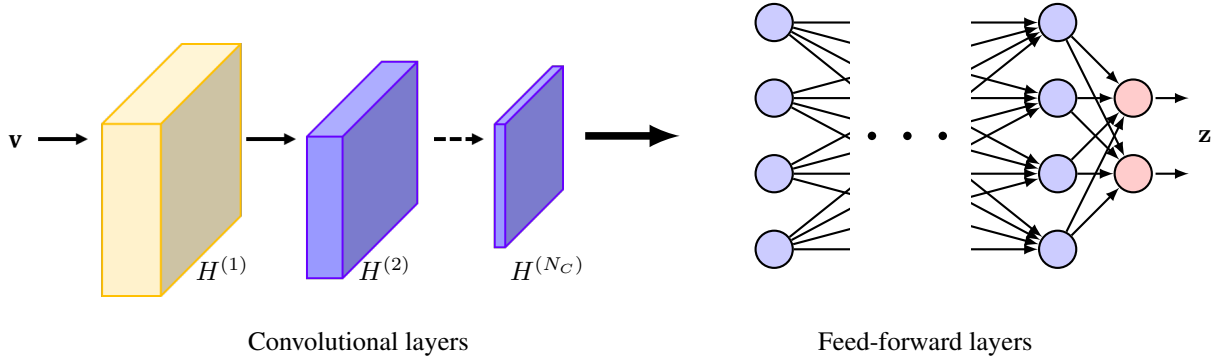


Figure 6: A schematic of the convolutional neural network (CNN), where  $N_C$  convolutional layers are followed by a few feed-forward layers to produce the output  $\mathbf{z}$  given the input  $\mathbf{v}$ .

### 2.2.3 Training of a neural network

The parameters  $\theta$  of a neural network, which can contain the weights and biases  $\{\{\mathbf{W}_i\}_{i=0}^{N_H}, \{\mathbf{b}_i\}_{i=0}^{N_H}\}$  and the set of kernels  $\{\{\Psi_i\}_{i=1}^{N(C)}\}$ , are learned from the data by minimizing the mismatch between the prediction from the network and the training dataset. In this paper, the Mean Squared Error (MSE) given by

$$J = \frac{1}{N_{\text{tr}}} \sum_{i=1}^{N_{\text{tr}}} \left( \mathbf{z}_i - \mathcal{M}_{\text{NN}}(\mathbf{v}_i; \theta) \right)^2 \quad (9)$$

is used as the cost function for the optimization problem. A regularization term can also be added to obtain sparsely connected network. Stochastic Gradient Descent (SGD) is commonly used to update the parameters during the optimization as follows

$$\theta_{k+1} \leftarrow \theta_k - \eta_k \frac{\partial J}{\partial \theta_k}, \quad (10)$$

where  $\eta_k$  is the step size at the  $k$ th iteration, also known as the learning rate and back propagation is used to estimate the derivatives  $\frac{\partial J}{\partial \theta^{(k)}}$  [57, 59]. In this paper, a modified version of this standard SGD, namely, the Adaptive Moment (Adam) [60, 61, 62] is used. In this algorithm, historical information of the gradients is used to retard movements in the direction of large historical gradients. A brief description of the Adam algorithm is provided in Appendix A.

**Remark:** The universal approximation theorem [63, 64, 65, 38] guarantees that MLP with at least one hidden layer and enough hidden neurons with differentiable activation functions is able to approximate any continuous function up

to a given accuracy level. In practice, the limitations are two-fold — (i) the training algorithm used to optimize the parameters of the network might be unable to find the optimal values; and (ii) required number of neurons in the hidden layer may be quite large. Hence, multiple hidden layers are used in practical applications.

### 3 Proposed Methodology

In this section, the proposed approach for the response calculation of an uncertain locally nonlinear dynamical system using neural networks is discussed first. Then, the datasets used in training and validation for the numerical examples are described.

#### 3.1 Response Calculation of Locally Nonlinear Uncertain Dynamical System

Consider a locally nonlinear dynamical system with governing differential equation in state-space form given by

$$\begin{aligned}\dot{\mathbf{X}}(t; \boldsymbol{\xi}) &= \mathbf{A}\mathbf{X}(t; \boldsymbol{\xi}) + \mathbf{B}\mathbf{w}(t) + \mathbf{L}\mathbf{g}(\bar{\mathbf{X}}(t; \boldsymbol{\xi}); \boldsymbol{\xi}), \quad \mathbf{X}(0) = \mathbf{x}_0; \\ \mathbf{Y}(t; \boldsymbol{\xi}) &= \mathbf{C}\mathbf{X}(t; \boldsymbol{\xi}) + \mathbf{D}\mathbf{w}(t) + \mathbf{E}\mathbf{g}(\bar{\mathbf{X}}(t; \boldsymbol{\xi}); \boldsymbol{\xi}),\end{aligned}\tag{11}$$

where  $\mathbf{X}(t; \boldsymbol{\xi}) \in \mathbb{R}^{n \times 1}$  is the state vector;  $\mathbf{A} \in \mathbb{R}^{n \times n}$  is the state matrix;  $\mathbf{w}(t) \in \mathbb{R}^{n_w \times 1}$  is the external force vector;  $\mathbf{B} \in \mathbb{R}^{n \times n_w}$  is the influence matrix for  $\mathbf{w}(t)$ ;  $\mathbf{g}(\cdot; \cdot) \in \mathbb{R}^{n_g \times n_g}$  is a nonlinear function of a subset of the state, (*i.e.*,  $\bar{\mathbf{X}}(t; \boldsymbol{\xi}) = \mathbf{G}\mathbf{X}(t; \boldsymbol{\xi})$  with  $\mathbf{G} \in \mathbb{R}^{n_g \times n}$  and  $n_g \ll n$ ) and the uncertain variable  $\boldsymbol{\xi}$  with known probability distribution;  $\mathbf{L} \in \mathbb{R}^{n \times n_g}$  is the influence matrix for the nonlinear function  $\mathbf{g}(\cdot; \cdot)$ ; and  $\mathbf{x}_0$  is the initial state vector. The output is denoted as  $\mathbf{Y}(t; \boldsymbol{\xi}) \in \mathbb{R}^{n_y \times 1}$ . The output influence matrices are  $\mathbf{C} \in \mathbb{R}^{n_y \times n}$ ,  $\mathbf{D} \in \mathbb{R}^{n_y \times n_w}$ , and  $\mathbf{E} \in \mathbb{R}^{n_y \times n_g}$  for the state vector  $\mathbf{X}(t; \boldsymbol{\xi})$ , external force  $\mathbf{w}(t)$ , and the uncertain and possibly nonlinear function  $\mathbf{g}(\cdot; \cdot)$ , respectively. For example, consider a multi-degree of freedom nonlinear mass-spring-damper system with governing equation

$$\mathbf{M}_s \ddot{\mathbf{u}}(t; \boldsymbol{\xi}) + \mathbf{C}_s \dot{\mathbf{u}}(t; \boldsymbol{\xi}) + \mathbf{K}_s \mathbf{u}(t; \boldsymbol{\xi}) + \mathbf{L}_s \mathbf{g}_s(\mathbf{u}(t; \boldsymbol{\xi}), \dot{\mathbf{u}}(t; \boldsymbol{\xi}); \boldsymbol{\xi}) = \mathbf{w}(t),\tag{12}$$

where  $\mathbf{u}(t; \boldsymbol{\xi})$  is the displacement vector;  $\mathbf{M}_s \in \mathbb{R}^{m \times m}$  is the mass matrix;  $\mathbf{C}_s \in \mathbb{R}^{m \times m}$  is the damping matrix;  $\mathbf{K}_s \in \mathbb{R}^{m \times m}$  is the stiffness matrix;  $\mathbf{L}_s \in \mathbb{R}^{m \times n_{g_s}}$  is the influence matrix of the nonlinear and uncertain vector  $\mathbf{g}_s(\cdot, \cdot; \cdot) \in \mathbb{R}^{n_{g_s} \times 1}$ . The state-space matrices for this system are as follows

$$\mathbf{X}(t; \boldsymbol{\xi}) = \begin{Bmatrix} \mathbf{u}(t; \boldsymbol{\xi}) \\ \dot{\mathbf{u}}(t; \boldsymbol{\xi}) \end{Bmatrix}, \quad \mathbf{A} = \begin{bmatrix} \mathbf{0} & \mathbf{I} \\ -\mathbf{M}_s^{-1}\mathbf{K}_s & -\mathbf{M}_s^{-1}\mathbf{C}_s \end{bmatrix}, \quad \mathbf{B} = \begin{Bmatrix} \mathbf{0} \\ \mathbf{M}_s^{-1}\mathbf{1} \end{Bmatrix}, \quad \mathbf{L} = \begin{Bmatrix} \mathbf{0} \\ -\mathbf{M}_s^{-1}\mathbf{L}_s \end{Bmatrix},\tag{13}$$

where  $\mathbf{I}$  is the identity matrix;  $\mathbf{0}$  is a matrix with all entries as zeros; and  $\mathbf{1}$  is a matrix with all entries as ones. A deterministic nominal linear dynamical system corresponding to this uncertain nonlinear dynamical system can be given by

$$\begin{aligned}\dot{\mathbf{x}}(t) &= \mathbf{A}\mathbf{x}(t) + \mathbf{B}\mathbf{w}(t), \quad \mathbf{x}(0) = \mathbf{x}_0; \\ \mathbf{y}(t) &= \mathbf{C}\mathbf{x}(t) + \mathbf{D}\mathbf{w}(t),\end{aligned}\tag{14}$$

where  $\mathbf{x}(t)$  and  $\mathbf{y}(t)$  are state and output of the nominal dynamical system, respectively.

The response of the original uncertain locally nonlinear dynamical system is expressed, next, as summation of the response of the nominal linear system  $\mathbf{x}(t)$  from (14) and a correction term  $\mathbf{x}_{\text{corr}}(t; \boldsymbol{\xi})$  due to the nonlinearity and uncertainty present in the system, *i.e.*,

$$\mathbf{X}(t; \boldsymbol{\xi}) = \mathbf{x}(t) + \mathbf{x}_{\text{corr}}(t; \boldsymbol{\xi}).\tag{15}$$

The response of the nominal linear system can be estimated using

$$\begin{aligned}\mathbf{x}(t) &= \exp(\mathbf{A}t)\mathbf{x}_0 + \int_0^t \mathbf{H}_B(t - \tau)\mathbf{w}(\tau)d\tau; \\ \mathbf{y}(t) &= \mathbf{C}\exp(\mathbf{A}t)\mathbf{x}_0 + \int_0^t \mathbf{C}\mathbf{H}_B(t - \tau)\mathbf{w}(\tau)d\tau + \mathbf{D}\mathbf{w}(t),\end{aligned}\tag{16}$$

where the impulse response function  $\mathbf{H}_B(t) = \exp(\mathbf{A}t)\mathbf{B}$ . Note that the convolution integral can be efficiently evaluated using the Fast Fourier Transform (FFT). However, the most challenging part is to estimate  $\mathbf{x}_{\text{corr}}(t)$ , which can be similarly written as

$$\begin{aligned}\mathbf{x}_{\text{corr}}(t; \boldsymbol{\xi}) &= \int_0^t \mathbf{H}_L(t - \tau)\mathbf{g}(\bar{\mathbf{X}}(\tau; \boldsymbol{\xi}); \boldsymbol{\xi}) d\tau; \\ \mathbf{Y}(t; \boldsymbol{\xi}) &= \mathbf{y}(t) + \underbrace{\int_0^t \mathbf{C}\mathbf{H}_L(t - \tau)\mathbf{g}(\bar{\mathbf{X}}(\tau; \boldsymbol{\xi}); \boldsymbol{\xi}) d\tau}_{=\mathbf{y}_{\text{corr}}(t; \boldsymbol{\xi})} + \mathbf{E}\mathbf{g}(\bar{\mathbf{X}}(\tau; \boldsymbol{\xi}); \boldsymbol{\xi}),\end{aligned}\tag{17}$$

where the impulse response function  $\mathbf{H}_L(t) = \exp(\mathbf{A}t)\mathbf{L}$  is due to the nonlinear function  $\mathbf{g}(\cdot, \cdot)$  and  $\mathbf{y}_{\text{corr}}(t; \boldsymbol{\xi})$  is the contribution to the output from  $\mathbf{g}(\cdot, \cdot)$ . Here,  $\mathbf{x}_{\text{corr}}(t; \boldsymbol{\xi})$  implicitly depends on  $\mathbf{X}(t; \boldsymbol{\xi})$  as can be seen in the solution of (17). An iterative and complex approach to solve (17) using FFT and Newton's method was proposed in [24] but requires  $\partial \mathbf{g} / \partial \mathbf{x}$  and an efficient breakup of the convolution sum to achieve a computational speedup. In this paper, instead, neural networks are employed to model a pseudoforce defined as

$$\mathbf{p}(t; \boldsymbol{\xi}) \approx \mathbf{g}(\bar{\mathbf{X}}(t; \boldsymbol{\xi}); \boldsymbol{\xi}). \quad (18)$$

Figure 7 shows the proposed approach with one-time calculation to estimate the nominal response  $\mathbf{x}(t)$  and repeated calculation using the neural network to estimate the response  $\mathbf{x}_{\text{corr}}(t; \boldsymbol{\xi})$ , where  $\bar{\mathbf{x}}(t) = \mathbf{G}\mathbf{x}(t)$  is also used as the input for the neural network. Note that,  $\mathbf{p}(t; \boldsymbol{\xi})$  is also the solution of a nonlinear Volterra integral equation of the second kind written in a non-standard form given by

$$\mathbf{p}(t; \boldsymbol{\xi}) - \mathbf{g}\left(\bar{\mathbf{x}}(t) + \int_0^t \mathbf{H}_L(t - \tau)\mathbf{p}(\tau; \boldsymbol{\xi}) d\tau; \boldsymbol{\xi}\right) = \mathbf{0}. \quad (19)$$

The solution of (19), however, requires an iterative strategy due to the nonlinearity [24, 16, 17].

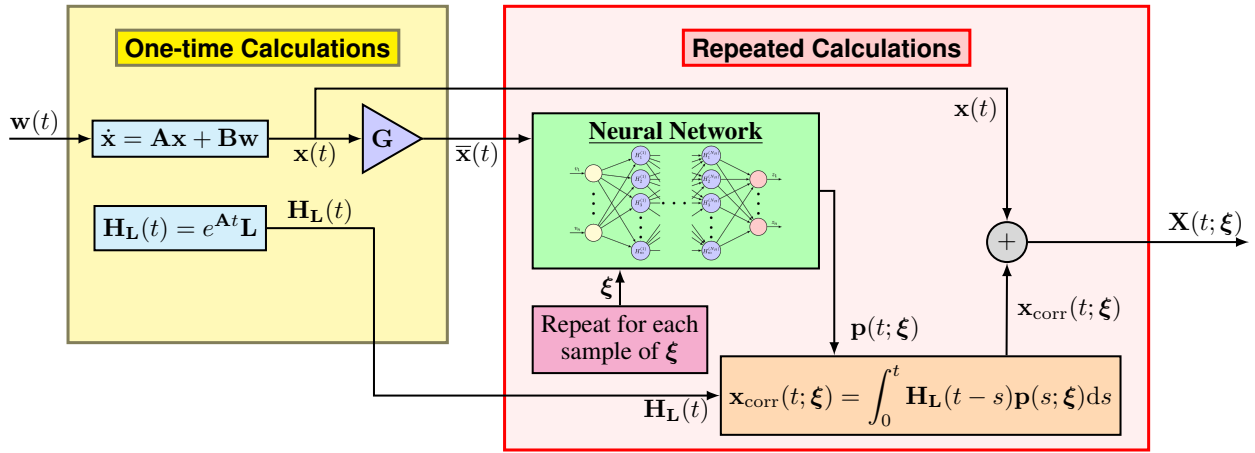


Figure 7: Implementation of the proposed approach for efficient uncertainty quantification showing one time calculation and repeated calculation components.

### 3.2 Datasets used in Training of the Neural Networks

To train these neural networks, two datasets, namely, the training dataset  $\mathcal{D}_{\text{tr}} = \left\{ \left\{ \mathbf{p}\left(t_i; \boldsymbol{\xi}_j^{(\text{tr})}\right) \right\}_{i=1}^{n_t}, \boldsymbol{\xi}_j^{(\text{tr})} \right\}_{j=1}^{N_{\text{tr}}}$  and

the validation dataset  $\mathcal{D}_{\text{val}} = \left\{ \left\{ \mathbf{p}\left(t_i; \boldsymbol{\xi}_j^{(\text{val})}\right) \right\}_{i=1}^{n_t}, \boldsymbol{\xi}_j^{(\text{val})} \right\}_{j=1}^{N_{\text{val}}}$  are generated by solving (19) at time instances  $\{t_i\}_{i=1}^{n_t}$

for random  $N_{\text{tr}}$  and  $N_{\text{val}}$  realizations of  $\boldsymbol{\xi}$ , respectively, where  $\{\boldsymbol{\xi}_j\}_{j=1}^{N_{\text{tr}}}$  and  $\{\boldsymbol{\xi}_j\}_{j=1}^{N_{\text{val}}}$  do not overlap. For neural networks,  $\boldsymbol{\xi}$  and  $\bar{\mathbf{x}}(t)$  are used for input  $\mathbf{v}$  and  $\mathbf{p}(t; \boldsymbol{\xi})$  is used as the output  $\mathbf{z}$  (see (3), (6), and Figure 6). The training dataset  $\mathcal{D}_{\text{tr}}$  is used to estimate the gradients and the validation dataset  $\mathcal{D}_{\text{val}}$  is used to monitor the validation Root Mean Squared Error (RMSE) defined as

$$\text{RMSE} = \frac{\sum_{i=1}^{N_{\text{val}}} \left\| \mathbf{p}\left(t; \boldsymbol{\xi}_j^{(\text{val})}\right) - \mathbf{p}_{\text{NN}}\left(t; \boldsymbol{\xi}_j^{(\text{val})}\right) \right\|_2}{\sum_{i=1}^{N_{\text{val}}} \left\| \mathbf{p}\left(t; \boldsymbol{\xi}_j^{(\text{val})}\right) \right\|_2}, \quad (20)$$

where  $\mathbf{p}\left(t; \boldsymbol{\xi}_j^{(\text{val})}\right)$  is the prediction using the neural network and  $\|\cdot\|_2$  is the Euclidean norm. For FNN and ResNet architectures, an iterative procedure is followed to select the number of hidden layers  $N_H$  and the number of neurons per hidden layer  $m$  [45], where  $m$  is increased gradually up to a maximum while a validation error is monitored. The number of hidden layers  $N_H$  is increased by one if a pre-chosen maximum neurons per layer is reached. The final



configuration is chosen that corresponds to the smallest validation error. For CNN, a similar procedure with the number of convolution layers is followed. The training of these neural networks require a few hours on a modern desktop. Once trained these networks produce inexpensive but accurate prediction of the response of the locally nonlinear dynamical system under uncertainty as the next three numerical examples show. The same trained network can be used even when the quantity of interest depends on different responses. Further, they can be also used for other applications such as design under uncertainty, sensitivity analysis, and so on.

## 4 Numerical Examples

Three numerical examples utilizing structures with increasing number of DOF are used in this section to illustrate the proposed approach. PyTorch [27] is used to implement the neural networks for the examples. For brevity, the dependence of the quantities on  $t$  and  $\xi$  are omitted in this section. In the examples, the accuracy of the estimates is measured using the Root Mean Squared Error (RMSE) given by  $\frac{\|\hat{\mathbf{y}} - \mathbf{y}\|_2}{\|\mathbf{y}\|_2}$ , where  $\hat{\mathbf{y}}$  is the estimated quantity and  $\mathbf{y}$  is the true response.

### 4.1 Example I: Two Degree-of-freedom Nonlinear Spring-Mass-Damper Model

A two DOF spring-mass-damper model with nonlinear damping is used in this example (see Figure 8). The equations

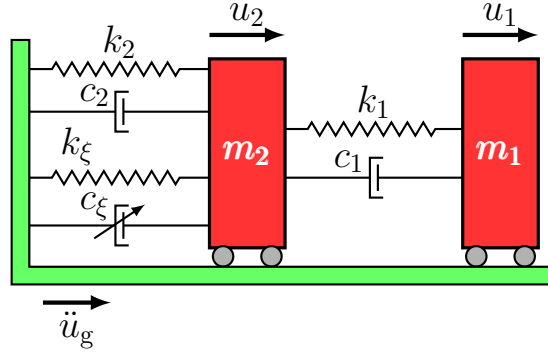


Figure 8: Two DOF spring-mass-damper model with uncertain stiffness  $k_\xi$  and nonlinear damping  $c_\xi$  used in Example I.

of motion for this model are given by

$$\begin{aligned} m_1 \ddot{u}_1 + c_1(\dot{u}_1 - \dot{u}_2) + k_1(u_1 - u_2) &= -m_1 \ddot{u}_g; \\ m_2 \ddot{u}_2 + c_1(\dot{u}_2 - \dot{u}_1) + c_2 \dot{u}_2 + c_\xi (\dot{u}_2)^3 + k_1(u_2 - u_1) + (k_2 + k_\xi)u_2 &= -m_2 \ddot{u}_g, \end{aligned} \quad (21)$$

where the state vector is  $\mathbf{X} = [u_1 \ u_2 \ \dot{u}_1 \ \dot{u}_2]^T$  and  $\ddot{u}_g$  is the ground acceleration. To generate the training and validation datasets, the following specifications are used:  $m_1 = 29,485$  kg,  $m_2 = 6,800$  kg,  $k_1 = 11,912$  kN/m,  $k_2 = 250$  kN/m,  $c_1 = 23.71$  kN·s/m, and  $c_2 = 4$  kN·s/m, where the parameters are selected from [66]. The uncertainty is assumed in the stiffness  $k_\xi$  and damping coefficient  $c_\xi$ . The probability distributions for these two parameters are shown in Table 1. The base excitation used is a stationary filtered white noise from a Kanai-Tajimi filter [67] that has a spectral density

$$S_{\ddot{u}_g \ddot{u}_g}(\omega) = \frac{S_0(4\zeta_g^2 \omega_g^2 \omega^2 + \omega_g^4)}{(\omega^2 - \omega_g^2)^2 + 4\zeta_g^2 \omega_g^2 \omega^2}, \quad (22)$$

where  $\omega_g = 17$  rad/s and  $\zeta_g = 0.3$  are chosen from [66]. The spectral intensity  $S_0$  is given by

$$S_0 = \sigma_w^2 \frac{0.03 \zeta_g}{\pi \omega_g (4\zeta_g^2 + 1)} g^2, \quad (23)$$

where  $g$  is the gravitational acceleration and  $\sigma_w = 2$  is selected to have a pronounced nonlinearity in the system response. In the state-space form of (11),  $\mathbf{L} = [0 \ 0 \ 0 \ -1/m_2]^T$  and  $g(\overline{\mathbf{X}}) = k_\xi u_2 + c_\xi (\dot{u}_2)^3$ , where  $\overline{\mathbf{X}} = [u_2 \ \dot{u}_2]^T$ .

Table 1: Probability distribution of the uncertain parameters in Example I.

Parameter	Distribution	Mean	Std. Dev.
$k_\xi$	Truncated Gaussian*	40 kN/m	10 kN/m
$c_\xi$	Lognormal	75 kN·(s/m) <sup>1/3</sup>	20 kN·(s/m) <sup>1/3</sup>

\* Truncated below at zero.

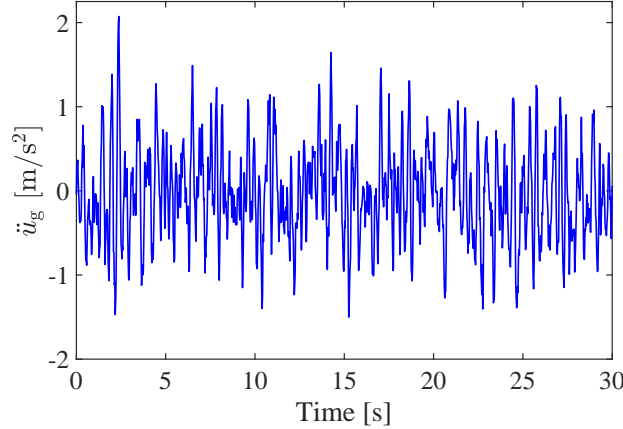


Figure 9: Base excitation generated using a Kanai-Tajimi filter in (22) and used in Example I.

#### 4.1.1 Results

The neural networks are used to model the uncertain nonlinear term  $p(t; \xi) = g(\bar{\mathbf{X}}) = k_\xi u_2 + c_\xi (\dot{u}_2^3)$ . The training dataset  $\mathcal{D}_{\text{tr}} = \left\{ \left\{ p(t_i; \xi_j^{(\text{tr})}) \right\}_{i=1}^{n_t}, \xi_j^{(\text{tr})} \right\}_{j=1}^{N_{\text{tr}}}$  is generated using  $N_{\text{tr}} = 250$  random samples of the uncertain parameters drawn from their respective probability distributions given in Table 1 and with a 20 Hz temporal sampling rate. For validation dataset  $\mathcal{D}_{\text{val}} = \left\{ \left\{ p(t_i; \xi_j^{(\text{val})}) \right\}_{i=1}^{n_t}, \xi_j^{(\text{val})} \right\}_{j=1}^{N_{\text{val}}}$ , separate  $N_{\text{val}} = 50$  random samples are used.

To select the number of neurons per layer  $m$  and total number of hidden layers  $N_H$  a procedure described in Section 3.2 is followed. Figure 10 shows 4 layers and 200 neurons per layer produces the smallest validation error with FNN architecture. The activation function is chosen as the sigmoid function  $\sigma_{\text{sigm}}(\cdot)$  (see (4)) as it gives the smallest validation RMSE. ResNet uses a similar configuration with a residual connection between the first and third layer. For CNN, a similar procedure is followed and  $N_C = 3$  one-dimensional convolution layers with kernels of length three followed by two feed-forward layers with  $n_t$  neurons each are used. The activation function for the convolution layers are chosen as the sigmoid function  $\sigma_{\text{sigm}}(\cdot)$ , whereas the feed-forward layers use the ELU activation  $\sigma_{\text{ELU}}(\cdot)$  (see (5)). Adam algorithm briefly described in Appendix A is used to train these networks with a learning rate of  $10^{-3}$ , which is gradually halved every 2000 iterations for training of FNN and ResNet but halved every 500 iterations for training of CNN subjected to a maximum iteration of 10000. This schedule of learning rate produces converged result from the optimization. The training of FNN and ResNet architectures took approximately 4 hrs. whereas the training of CNN took approximately 6 hrs. Note that these trainings are performed on CPU (central processing unit). However, by performing them on GPU (graphics processing unit) the training time can be significantly reduced. At the conclusion of training, the trained network is chosen as the network that produces the smallest validation RMSE. This is equivalent to an early stopping criterion [68] commonly used in machine learning applications with infinite patience and subject to a maximum iteration count. Table 2 shows the validation RMSE using each of the three architectures, where CNN produces the smallest error as it implements a sharing of the network parameters. Figure 11 shows the estimated  $p(t; \xi)$  using these architectures for one realization of the uncertain parameters in the validation dataset  $\mathcal{D}_{\text{val}}$ .

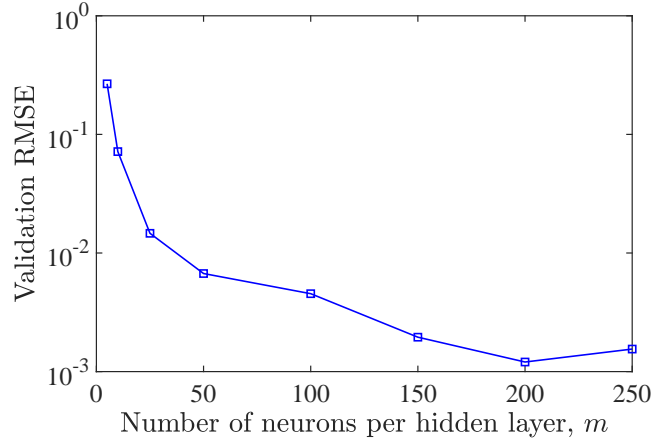


Figure 10: The validation RMSE decreases as more neurons are added to four hidden layers in FNN in Example I.

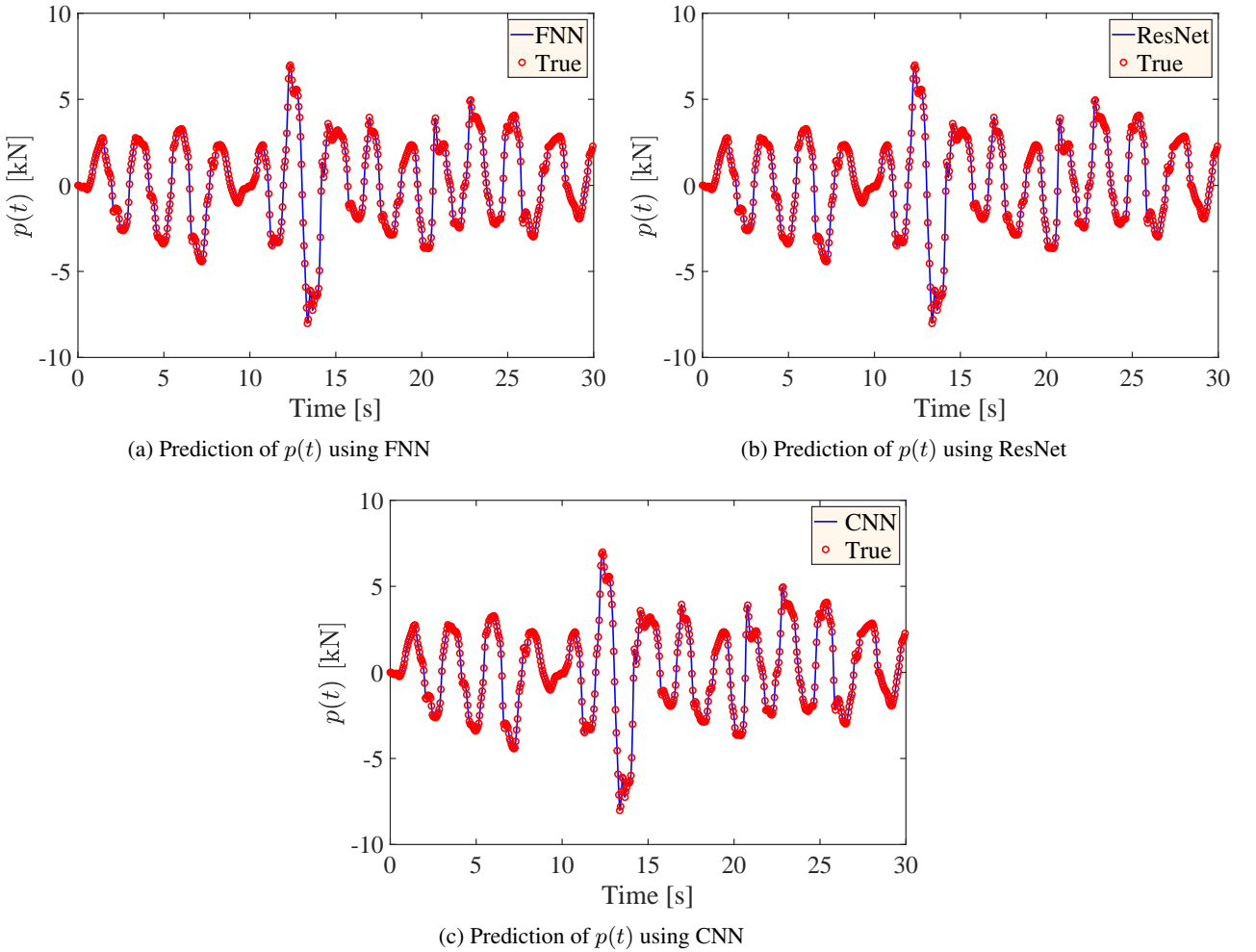


Figure 11: Comparison of predictions from three different neural network architectures for a realization of the uncertainty in the validation dataset  $\mathcal{D}_{\text{val}}$  in Example I. The true solution is obtained by solving (19).

Next, the mean and standard deviation of the displacement  $u_2$  of the base mass  $m_2$  are estimated using the proposed approach with  $N = 10^5$  random samples. Figure 12 shows the result and compares to the mean displacement obtained

Table 2: Validation RMSE for  $g(\bar{\mathbf{X}})$  using three different architectures for the neural networks in Example I.

NN architecture	Validation RMSE
FNN	$1.9506 \times 10^{-3}$
ResNet	$3.2809 \times 10^{-3}$
CNN	$1.2765 \times 10^{-3}$

Table 3: RMSE of mean and standard deviation of the base displacement  $u_2$  using three different architectures for the neural networks in Example I.

NN architecture	RMSE of mean	RMSE of std dev
FNN	$1.1369 \times 10^{-3}$	$8.5926 \times 10^{-3}$
ResNet	$1.2870 \times 10^{-3}$	$8.7527 \times 10^{-3}$
CNN	$1.0753 \times 10^{-3}$	$8.1803 \times 10^{-3}$

from solving Table 3 reports the RMSE of the mean and standard deviation of the response  $u_2$ , which shows that the CNN architecture slightly outperforms the others. Also, the validation RMSE for the prediction of standard deviation is larger as it is more difficult to estimate this statistic. Once trained the FNN takes a total 3.94 min. in for predicting responses for  $10^5$  different realizations of the uncertainty. ResNet and CNN take 4.19 min. and 1.82 min., respectively, in total for  $10^5$  evaluations. On the other hand, to solve (19) using a computationally efficient method [16] takes 1.27 hrs. in total for these evaluations. Note that MATLAB's ode45, a standard nonlinear solver, which does not have any associated one-time cost, however, takes 6.37 s for one evaluation and hence it would take approximately 7 days for  $10^5$  evaluations if this solver is used. The difference in computational cost is even more pronounced for complex structures as shown in the next two examples. Note that a desktop with octa-core Intel i9 – 9900k @3.60 GHz processor and 64 GB of RAM and running Wondows 10 is used to estimate the computation time.

## 4.2 Example II: 11 Story Base Isolated Building

In the second example, a 11-story 2-bay structural model with a hysteretic base isolation layer as shown in Figure 13a is used. The base layer is assumed rigid in-plane and moving horizontally. The beams are modeled using consistent mass matrix and weights of the columns are neglected. The governing equations of this structure are given by

$$\begin{aligned} \mathbf{M}_s \ddot{\mathbf{u}}_s + \mathbf{C}_s \dot{\mathbf{u}}_s + \mathbf{K}_s \mathbf{u}_s &= -\mathbf{M}_s \mathbf{r} \ddot{u}_g + \mathbf{C}_s \mathbf{r} \dot{u}_b + \mathbf{K}_s \mathbf{r} u_b; \\ m_b \ddot{u}_b + (c_b + \mathbf{r}^T \mathbf{C}_s \mathbf{r}) \dot{u}_b + (k_b + \mathbf{r}^T \mathbf{K}_s \mathbf{r}) u_b + f_b &= -m_b \ddot{u}_b + \mathbf{r}^T \mathbf{C}_s \mathbf{r} \dot{\mathbf{u}}_s + \mathbf{r}^T \mathbf{K}_s \mathbf{r} \mathbf{u}_s, \end{aligned} \quad (24)$$

where  $\mathbf{M}_s$  is the mass matrix,  $\mathbf{C}_s$  is the damping matrix, and  $\mathbf{K}_s$  is the stiffness matrix of the superstructure;  $\mathbf{u}$  is the displacement of the superstructure relative to the ground;  $\ddot{u}_g$  is the ground acceleration; and the influence vector for the ground acceleration is  $\mathbf{r} = [1, 0, 0, \dots, 1, 0, 0]^T$ , where the ones correspond to the horizontal displacement DOF. Note that the column weights are neglected but for the beams consistent mass matrix is used. The superstructure uses 33 nodes and three DOF per node. Hence, the combined structure with another DOF for the base layer has a total 100 DOF. The above equation can be converted to the state-space formulation in (11) using  $\mathbf{X} = [\mathbf{u}_s^T \ u_b \ \dot{\mathbf{u}}_s^T \ \dot{u}_b]^T$ . Rayleigh damping with 3% damping ratios for the 1<sup>st</sup> and 10<sup>th</sup> superstructure modes is assumed. A record of the 1940 El Centro earthquake measured at the N-S Imperial Valley Irrigation District substation with peak ground acceleration  $0.348g$  is used as the ground acceleration  $\ddot{u}_g$ .

The nonlinearity is assumed in the restoring force of the hysteretic base layer described using the Bouc-Wen model (see Figure 13b) [69], which gives the sum of the base layer restoring and damping forces as

$$g(u_b, \dot{u}_b) = f_b = c_b \dot{u}_b + k_{\text{post}} u_b + \alpha z_{\text{hyst}}, \quad (25)$$

where  $c_b$  is the base layer damping coefficient;  $k_{\text{pre}}$  and  $k_{\text{post}}$  are pre- and post-yield stiffness, respectively;  $\alpha = Q_y(1 - r_k)$  is the peak of the nonelastic force;  $Q_y$  is the yield force of the hysteretic layer;  $r_k = k_{\text{post}}/k_{\text{pre}}$  is the hardening ratio; and  $z_{\text{hyst}}$  is an auxiliary variable that describes the evolution of the hysteretic loop. The evolution of  $z_{\text{hyst}}$  is given by

$$\dot{z}_{\text{hyst}} = A \dot{u}_b - \beta \dot{u}_b |z_{\text{hyst}}| - \gamma z_{\text{hyst}} |\dot{u}_b|, \quad (26)$$

where  $A = 2\beta = 2\gamma = k_{\text{pre}}/Q_y$  produces identical loading and unloading curves [66, 70] with  $z_{\text{hyst}}$  in  $[-1, 1]$ . Four parameters, namely,  $c_b$ ,  $k_{\text{post}}$ ,  $Q_y$ , and  $r_k$  are assumed uncertain. The assumed probability distributions of these parameters are given in Table 4.

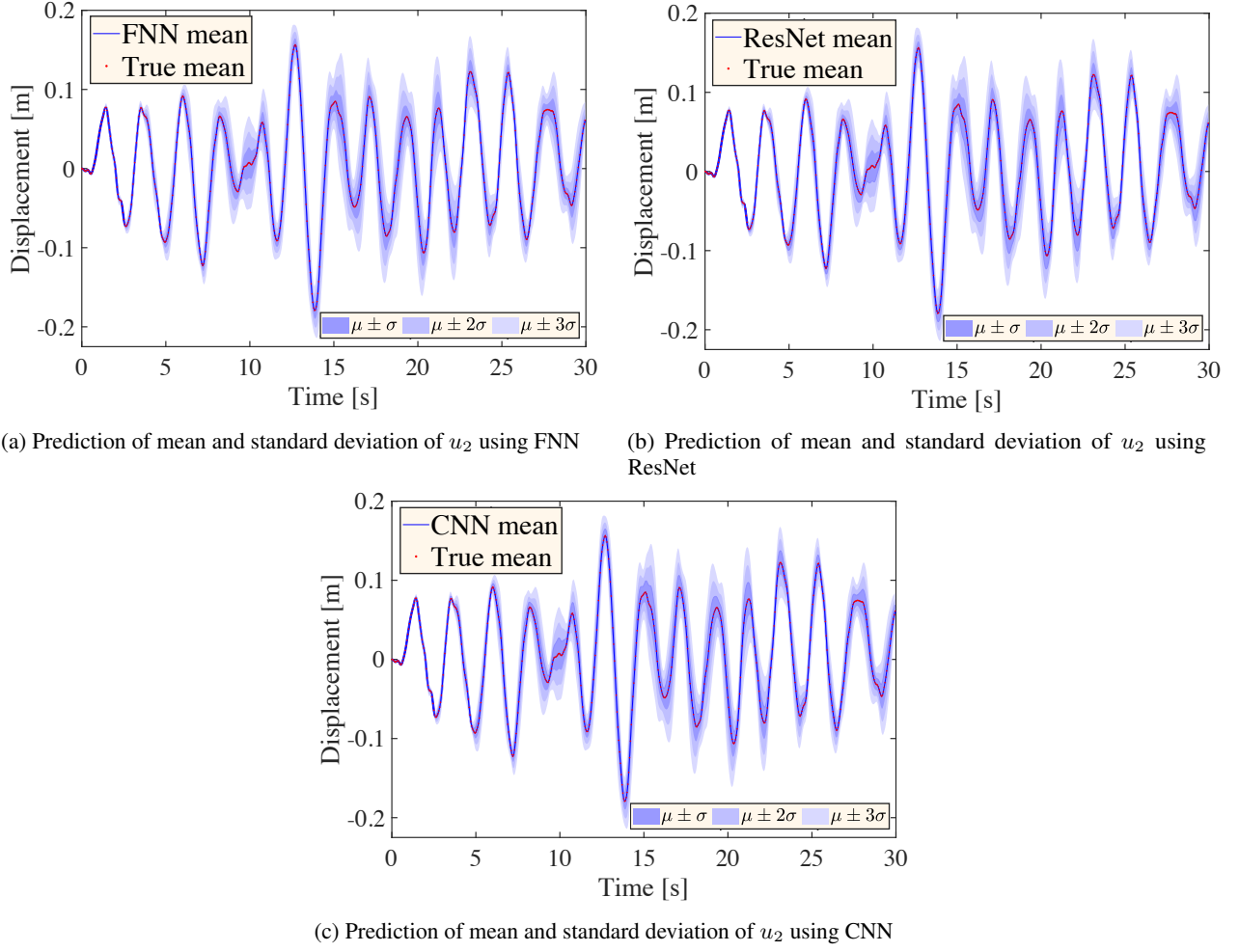


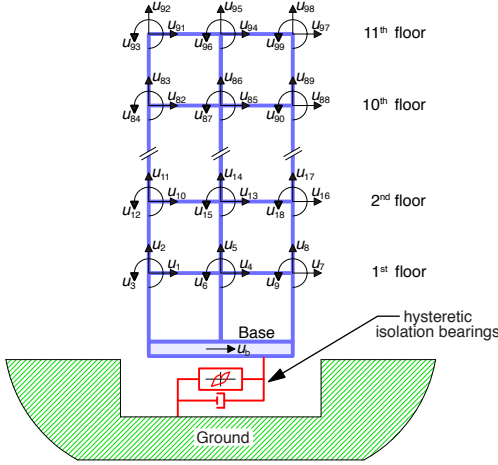
Figure 12: Prediction of the mean and standard deviations of  $u_2$  from three different neural network architectures using  $10^5$  realizations of the uncertainty in Example I. The mean responses from the neural networks are compared with mean estimated from solving (19) for  $10^5$  realizations of the uncertainty. The shaded regions show combinations of mean  $\mu$  and standard deviation  $\sigma$  of the response.

Table 4: Probability distribution of the uncertain parameters in Example II.

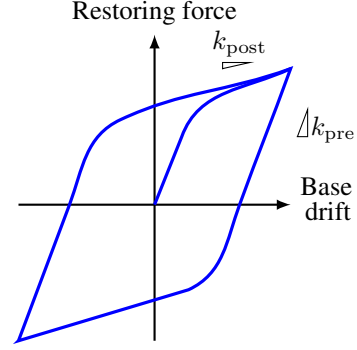
Parameter	Distribution	Mean	Std. Dev.
$k_{\text{post}}$	Lognormal	250 kN/m	20 kN/m
$c_b$	Truncated Gaussian*	3.5 kN·s/m	0.25 kN·s/m
$Q_y$ (%) <sup>†</sup>	Uniform	5.0	0.5774
$r_k$	Uniform	0.1875	0.0361

\* Truncated below at zero.

<sup>†</sup> in % of the total weight of the structure.



(a) A 100 degree-of-freedom structure with a hysteretic base isolation layer.



(b) Bouc-Wen model for hysteresis.

Figure 13: An 11-story 2-bay 100 degree-of-freedom structure with a hysteretic base isolation layer described using the Bouc-Wen hysteresis model is used in Example II.

#### 4.2.1 Results

In this example, the neural networks are used to model the uncertain nonlinear restoring force in the base layer as

$p(t; \xi) = f_b$ . The training dataset  $\mathcal{D}_{tr} = \left\{ \left\{ p(t_i; \xi_j^{(tr)}) \right\}_{i=1}^{n_t}, \xi_j^{(tr)} \right\}_{j=1}^{N_{tr}}$  is generated using  $N_{tr} = 450$  random samples of the uncertain parameters drawn from their respective probability distributions given in Table 4 and with a 20 Hz temporal sampling rate. For validation dataset  $\mathcal{D}_{val} = \left\{ \left\{ p(t_i; \xi_j^{(val)}) \right\}_{i=1}^{n_t}, \xi_j^{(val)} \right\}_{j=1}^{N_{val}}$ , separate  $N_{val} = 50$

random samples are used. A similar procedure to the previous example is followed here to select the number of neurons per layer as  $m = 100$  and total number of hidden layers as  $N_H = 4$  in the FNN network. The activation function is chosen as the hyperbolic tangent function  $\sigma_{\tanh}(\cdot)$  (see (4)) as it gives the smallest validation RMSE. ResNet uses a similar configuration with a residual connection between the first and third layer as this residual connection gives the smallest error among other residual connections. For CNN, a similar procedure is followed and  $N_C = 3$  one-dimensional convolution layers with kernels of length three followed by two feed-forward layers with  $n_t$  neurons in each of these layers are used. The activation function for the convolution layers are chosen as the hyperbolic tangent function  $\sigma_{\tanh}(\cdot)$ , whereas the feed-forward layers use the ELU activation  $\sigma_{ELU}(\cdot)$ . A learning rate of  $10^{-3}$  that is gradually halved every 2000 iterations for training of FNN and ResNet and halved every 500 iterations for training of CNN subjected to a maximum iteration of 10000 is used to train these networks using the Adam algorithm (see Appendix A). The training of FNN and ResNet networks takes approximately 3.5 hours, whereas the training of CNN network takes approximately 6 hours. The network parameters that produces the smallest validation RMSE is selected as the trained network at the end of training, which is equivalent to an early stopping criterion [68]. The validation RMSE using these three architectures are given in Table 5, which shows that the CNN provides the smallest validation RMSE. Figure 14 shows the estimated  $p(t; \xi) = f_b$  using these architectures for one realization of the uncertain parameters in the validation dataset  $\mathcal{D}_{val}$ .

Figure 15 compares the mean of the horizontal roof acceleration  $\ddot{u}_{97}$  for  $N = 10^5$  random samples of the uncertain parameters in Table 4 obtained from the proposed use of the neural networks with the mean estimated from solving (19). The figure also shows the estimated standard deviation of the response. Table 6 shows the RMSEs in the mean and standard deviation estimates. Similar to the previous example CNN produces the smallest error as it avoids overfitting by parameter sharing as described in Section 2.2.2. On the other hand, ResNet gives validation RMSE one order of magnitude larger than CNN showing that modeling the residual does not provide any advantage in this approach. The same trained CNN is further used to estimate the mean and standard deviation of the roof displacement  $u_{97}$  with  $N = 10^5$  realizations of the uncertain parameters (see Figure 16). Once trained the FNN, ResNet, and CNN take a total 1.13 hrs., 1.13 hrs., and 1.12 hrs., respectively, for predicting responses for  $10^5$  different realizations of the uncertainty. On the other hand, in this example solving (19) using a computationally efficient method [16] takes 15.33 hrs. in total

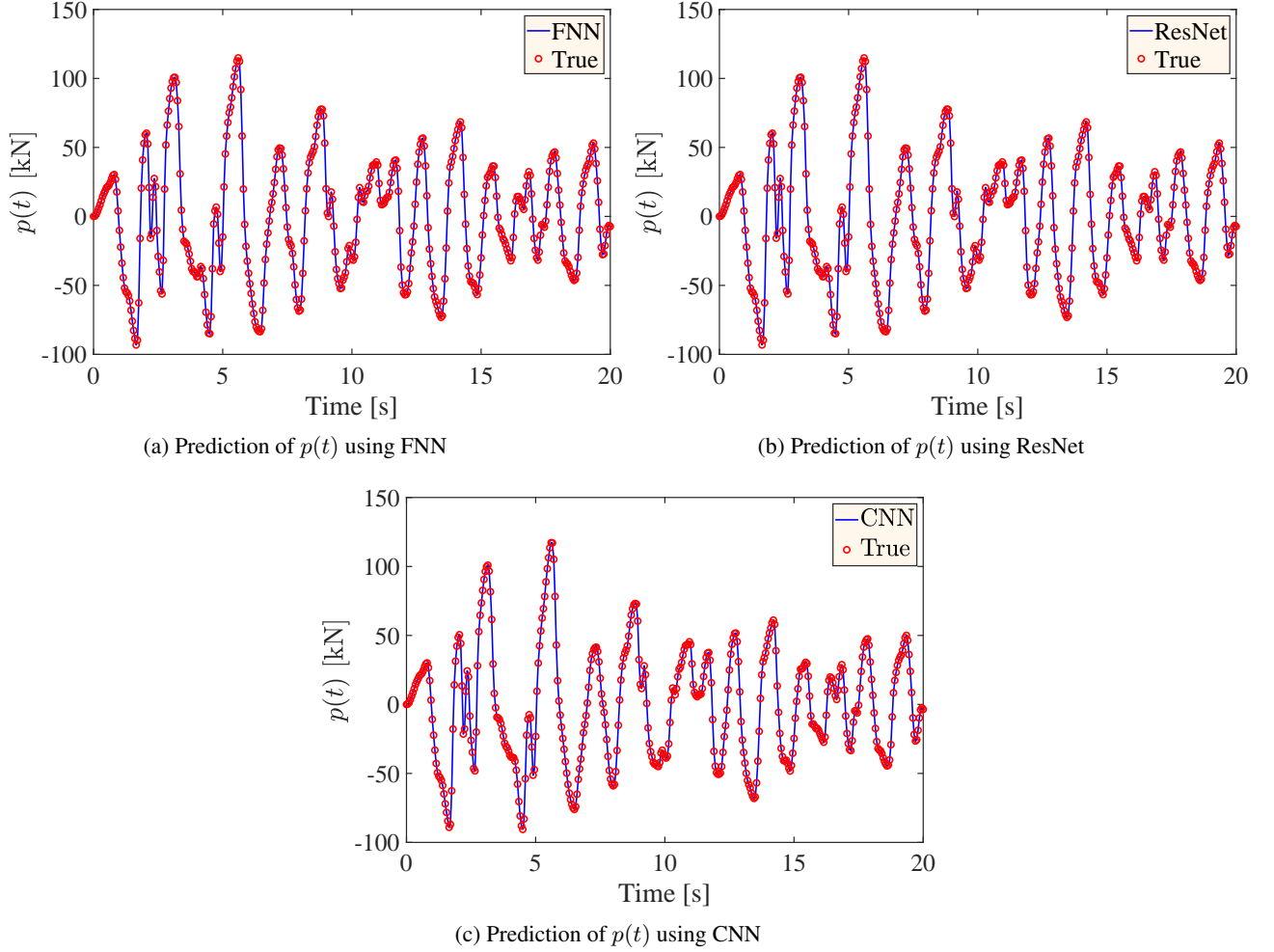


Figure 14: Comparison of predictions from three different neural network architectures for a realization of the uncertainty in the validation dataset  $\mathcal{D}_{\text{val}}$  in Example II. The true solution is obtained by solving (19).

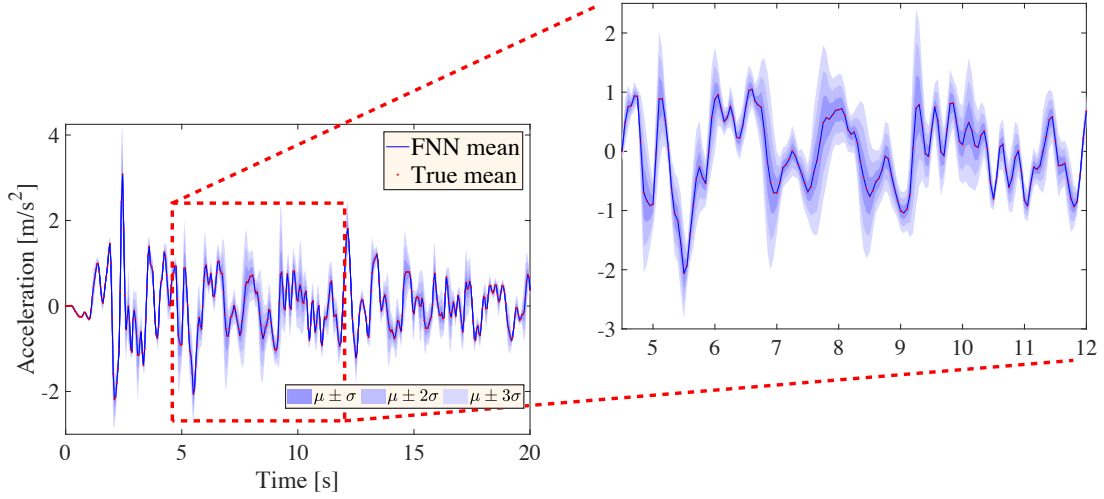
for these  $10^5$  evaluations. A standard nonlinear solver, MATLAB’s `ode45`, however, takes 12.98 s for one evaluation and hence it would take approximately 15 days for  $10^5$  evaluations if this solver is used.

Table 5: Validation RMSE for the isolator force  $f_b$  using three different architectures for the neural networks in Example II.

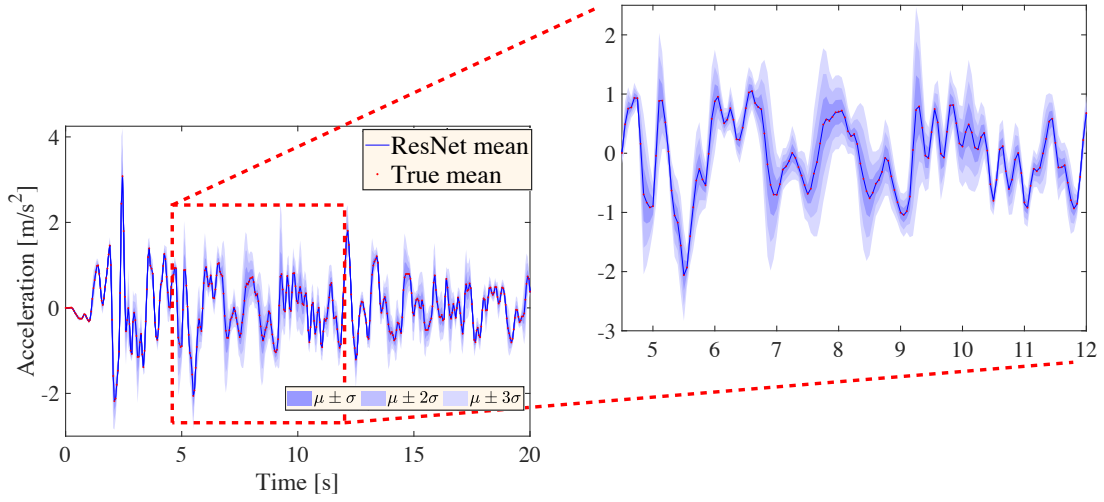
NN architecture	Validation RMSE
FNN	$2.8954 \times 10^{-3}$
ResNet	$1.2112 \times 10^{-2}$
CNN	$1.4874 \times 10^{-3}$

### 4.3 Example III: 1623 Degree-of-freedom Three-Dimensional Wind-Excited Structure

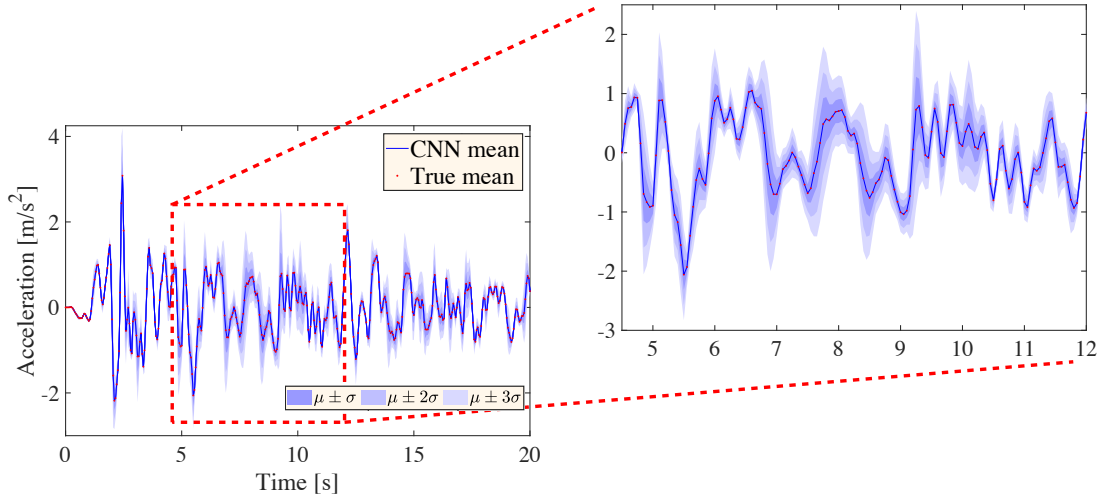
The third example uses a 20-story moment-resisting building frame with 1623 DOF adapted from [71], where three nonlinear Tuned Mass Dampers (TMDs) are attached to its roof. The dimensions of the building are shown in Figure 17. Its bottom five stories have  $5 \times 3$  bay. However, next five stories are reduced to  $3 \times 2$  bay and the last ten stories to  $2 \times 2$  bay. The building has cross braces to provide extra stiffness against lateral bending and torsion. The beams and columns in the building are modeled using the Euler-Bernoulli beam theory and the beam-column joints as rigid.



(a) Prediction of mean and standard deviation of the horizontal roof acceleration using FNN



(b) Prediction of mean and standard deviation of the horizontal roof acceleration using ResNet



(c) Prediction of mean and standard deviation of the horizontal roof acceleration using CNN

Figure 15: Prediction of the mean and standard deviations of the horizontal roof acceleration  $\ddot{u}_{97}$  from three different neural network architectures using  $10^5$  realizations of the uncertainty in Example II with response in  $[4.5, 12]$  s zoomed in. The mean responses from the neural networks are compared with mean estimated from solving (19) for  $10^5$  realizations of the uncertainty. The shaded regions show combinations of mean  $\mu$  and standard deviation  $\sigma$  of the response.



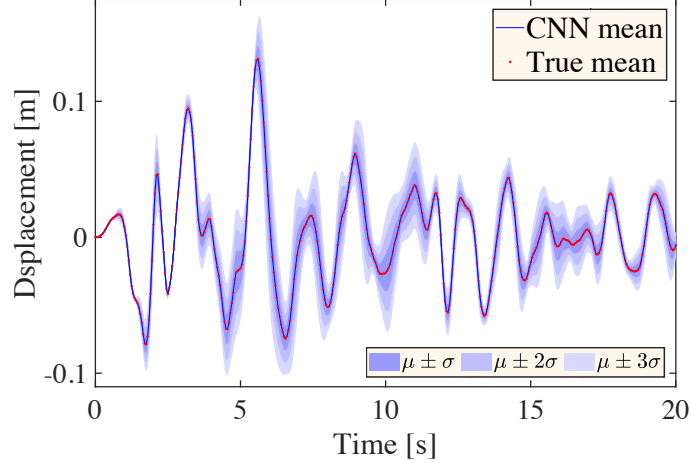


Figure 16: Prediction of the mean and standard deviations of horizontal roof displacement  $u_{97}$  from three different neural network architectures using  $10^5$  realizations of the uncertainty in Example I. The mean responses from the neural networks are compared with mean estimated from solving (19) for  $10^5$  realizations of the uncertainty. The shaded regions show combinations of mean  $\mu$  and standard deviation  $\sigma$  of the response.

Table 6: RMSE of mean and standard deviation of the horizontal roof acceleration  $\ddot{u}_{97}$  using three different architectures for the neural networks in Example II.

NN architecture	RMSE of mean	RMSE of std dev
FNN	$1.1369 \times 10^{-3}$	$8.5926 \times 10^{-3}$
ResNet	$1.2870 \times 10^{-3}$	$8.7527 \times 10^{-3}$
CNN	$1.0753 \times 10^{-3}$	$8.1803 \times 10^{-3}$

The building has 1620 DOF without the TMDs and its first six natural frequencies are summarized in Table 7. The

Table 7: First six natural frequencies of the 1623 DOF building used in Example III.

Mode No.	Mode type	Frequency (Hz)
1 <sup>st</sup>	$y$ -direction	0.5718
2 <sup>nd</sup>	$x$ -direction	0.5893
3 <sup>rd</sup>	torsional	0.9363
4 <sup>th</sup>	$y$ -direction	1.3632
5 <sup>th</sup>	$x$ -direction	1.5346
6 <sup>th</sup>	torsional	2.0292

building is subjected to a wind excitation from the northeast direction at an angle of  $30^\circ$  from east, which is modeled as a narrowband filtered Gaussian white noise filtered through a  $16^{\text{th}}$  order band-pass Butterworth filter with cutoff frequencies set at 1.2 times smaller and larger than the fundamental natural frequency. This choice of wind load excites the fundamental modes in the  $x$ - and  $y$ -directions, and in torsion. The wind excitation is shaped according to a power law model that is proportional to its height to the power 0.3 [72]. The damping forces in the three TMDs are assumed to follow a power law model given by

$$g(\dot{u}) = f_{\text{TMD}} = c_1 \dot{u} + c_2 |\dot{u}|^\beta \text{sgn}(\dot{u}), \quad (27)$$

where  $u$  is the displacement of the TMD relative to the roof; and the damping coefficients  $c_1$ ,  $c_2$ , and the exponent  $\beta$  are assumed uncertain with their distributions shown in Table 8.

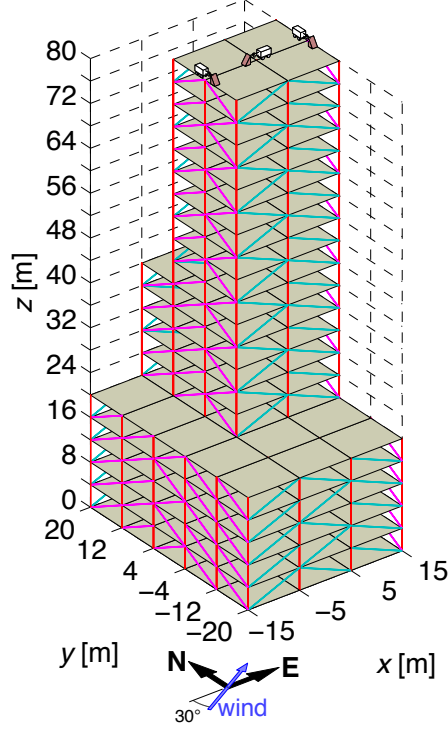


Figure 17: A 20-story building model with three tuned mass dampers at its roof used in Example III.

Table 8: Probability distribution of the uncertain parameters in Example III.

Parameter	Distribution	$x$ TMD		$y$ TMDs	
		Mean	Std. Dev.	Mean	Std. Dev.
$c_1$ [kN·s/m]	Gaussian	225	150	120	80
$c_2$ [kN·(s/m) $^\beta$ ]	Lognormal	27.5	12.5	20.0	10.0
$\beta$	Lognormal	0.85	0.20	0.85	0.20

#### 4.3.1 Results

In this example, the neural networks are used to model the uncertain nonlinear forces in the TMDs on the roof as

$p(t; \xi) = f_{\text{TMD}}$ . The training dataset  $\mathcal{D}_{\text{tr}} = \left\{ \left\{ p(t_i; \xi_j^{(\text{tr})}) \right\}_{i=1}^{n_t}, \xi_j^{(\text{tr})} \right\}_{j=1}^{N_{\text{tr}}}$  is generated using  $N_{\text{tr}} = 250$  random samples of the uncertain parameters drawn from their respective probability distributions given in Table 8 and with a 20 Hz temporal sampling rate. For validation dataset  $\mathcal{D}_{\text{val}} = \left\{ \left\{ p(t_i; \xi_j^{(\text{val})}) \right\}_{i=1}^{n_t}, \xi_j^{(\text{val})} \right\}_{j=1}^{N_{\text{val}}}$ , separate  $N_{\text{val}} = 50$

random samples are used. A similar procedure to the previous example is followed here to select the number of neurons per layer  $m = 200$  and total number of hidden layers  $N_H = 4$  in the FNN network. The activation function is chosen as the hyperbolic tangent function  $\sigma_{\text{tanh}}(\cdot)$  (see (4)) as it gives the smallest validation RMSE. ResNet uses a similar configuration with a residual connection between the first and third layer as other residual connections do not provide smaller validation RMSE. For CNN, a similar procedure is followed and  $N_C = 3$  one-dimensional convolution layers with kernels of length three followed by two feed-forward layers with  $n_t$  neurons in each of these layers are used. The activation function for the convolution layers are chosen as the hyperbolic tangent function  $\sigma_{\text{tanh}}(\cdot)$ , whereas the feed-forward layers use the ELU activation  $\sigma_{\text{ELU}}(\cdot)$ . These networks are trained using the Adam algorithm (see Appendix A) with a learning rate of  $10^{-3}$ , which is gradually halved every 2000 iterations for training of FNN and ResNet but halved every 500 iterations for training of CNN subjected to a maximum iteration of 10000. The training of FNN and ResNet networks takes approximately 4 hours each, whereas the training of CNN networks takes approximately 6 hours each.

The network parameters that produces the smallest validation RMSE is selected as the trained network at the end of training, which is equivalent to an early stopping criterion [68]. The validation RMSE using these three architectures are given in Table 9, which shows that the CNN provides the smallest validation RMSE as it prevents overfitting by parameter sharing. Figure 18 shows that the estimated force  $p_x(t; \xi) = f_{\text{TMD}}^x$  in the  $x$ -direction TMD using these architectures for one realization of the uncertain parameters in the validation dataset  $\mathcal{D}_{\text{val}}$  matches the true values.

Table 9: Validation RMSE for the TMD forces using three different architectures for the neural networks in Example III.

TMD	NN architecture	Validation RMSE
$x$ -direction TMD	FNN	$6.3901 \times 10^{-4}$
	ResNet	$3.0472 \times 10^{-3}$
	CNN	$2.0155 \times 10^{-4}$
$y$ -direction TMD#1	FNN	$8.2597 \times 10^{-4}$
	ResNet	$2.9137 \times 10^{-3}$
	CNN	$4.3792 \times 10^{-4}$
$y$ -direction TMD#2	FNN	$1.2655 \times 10^{-3}$
	ResNet	$1.8165 \times 10^{-3}$
	CNN	$6.4929 \times 10^{-4}$

Table 10: RMSE of mean and standard deviation of the roof accelerations in  $x$ - and  $y$ -directions using three different architectures for the neural networks in Example III.

Roof acceleration	NN architecture	RMSE of mean	RMSE of std dev
$x$ -direction	FNN	$2.6617 \times 10^{-4}$	$4.9477 \times 10^{-3}$
	ResNet	$7.4273 \times 10^{-4}$	$2.1737 \times 10^{-2}$
	CNN	$2.6451 \times 10^{-4}$	$3.6935 \times 10^{-3}$
$y$ -direction	FNN	$2.2522 \times 10^{-4}$	$1.2896 \times 10^{-2}$
	ResNet	$3.1833 \times 10^{-3}$	$2.0854 \times 10^{-2}$
	CNN	$5.3049 \times 10^{-4}$	$1.1705 \times 10^{-2}$

Figure 19 and 20 compare the mean of the roof acceleration in the  $x$ - and  $y$ -directions, respectively, for  $N = 10^5$  random samples of the uncertain parameters in Table 8 obtained from the proposed use of neural networks with mean estimated from solving (19). The figures also show the estimated standard deviation of the responses. Table 10 shows the RMSEs in the mean and standard deviation estimates of the roof accelerations in both  $x$ - and  $y$ -directions. Similar to the previous example, CNN produces the smallest error as it avoids overfitting by parameter sharing as described in Section 2.2.2. On the other hand, ResNet gives validation RMSE much larger than CNN showing that modeling the residual does not provide any advantage in this method. The RMSE in standard deviation is also higher as it is a difficult statistic to estimate compared to the mean. Note that the same trained networks are used to estimate the mean and standard deviation of accelerations in both  $x$ - and  $y$ -directions. Once trained the FNN, ResNet, and CNN take a total 2.96 hrs., 2.97 hrs., and 2.92 hrs., respectively, for predicting responses from  $10^5$  different realizations of the uncertainty. On the other hand, in this example solving (19) using a computationally efficient method [16] takes 30.23 hrs. for these evaluations. A standard nonlinear solver, MATLAB’s `ode45`, however, takes 14.20 min. for one evaluation and hence it would take approximately 2.74 yrs. (projected) for  $10^5$  evaluations if this solver is used, which is impractical. Note that the same desktop as in the previous examples is used to compute the computational timings.

## 5 Conclusions

In structural engineering, local nonlinearities often exist in structures like buildings, bridges, or spacecrafts. For these dynamical systems, the computational cost of uncertainty quantification can be significantly large if a nonlinear solver is used. In this paper, the response of a locally nonlinear dynamical system is divided into response of a nominal linear system and response from a pseudoforce that arises from the uncertainty and local nonlinearity. Recently, neural networks have become popular for representing a functional relationship due to their high level of expressiveness. Further, with the availability of advanced computational resources and open-sourced packages like

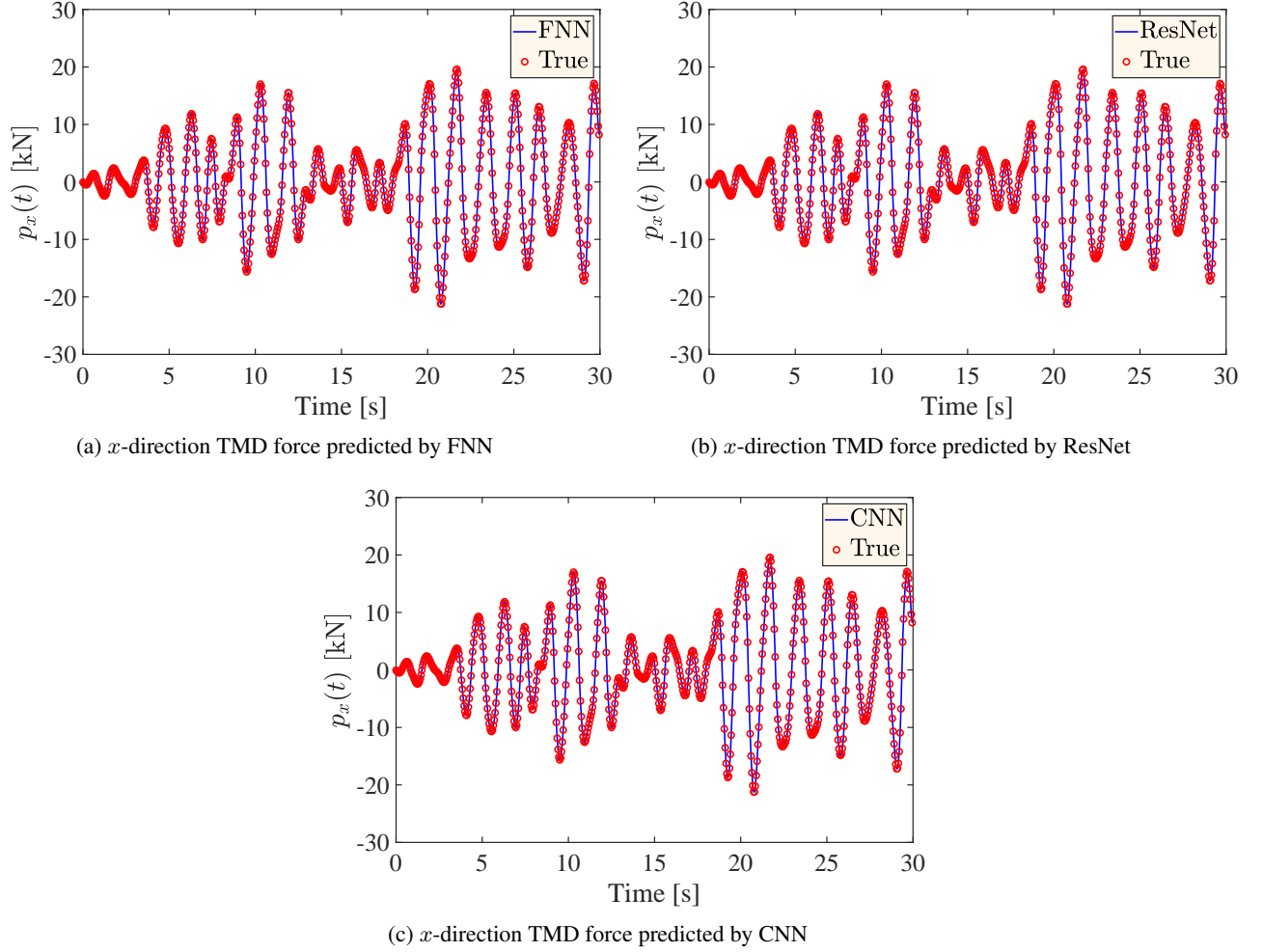


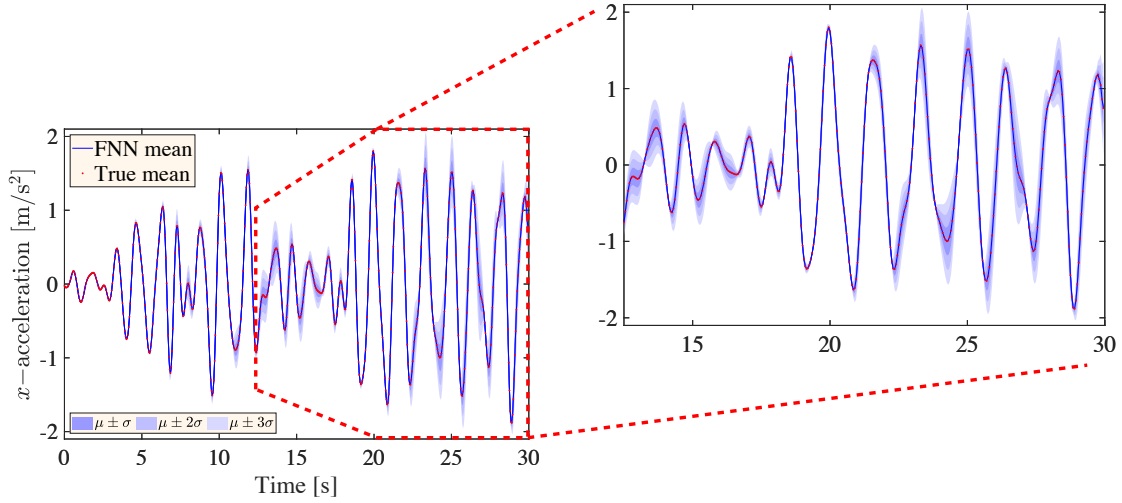
Figure 18: Comparison of predictions of the  $x$ -direction TMD force from three different neural network architectures for a realization of the uncertainty in the validation dataset  $\mathcal{D}_{\text{val}}$  in Example III. The true solution is obtained by solving (19).

PyTorch and TensorFlow the training of neural networks have become possible on a desktop. In this paper, three different architectures of these neural networks are investigated to predict the pseudoforce in the second part of the response from the nonlinearity and uncertainty present in the system. Three numerical examples with DOF ranging from two to 1623 are used to illustrate the efficacy of the proposed approach. These examples show that the neural networks can accurately model the pseudoforces and the total response of the system. Once trained these neural networks are efficiently used for estimating statistics of the response under uncertainty. The computational efficiency will be further pronounced for more complex engineering systems, which will be investigated in future.

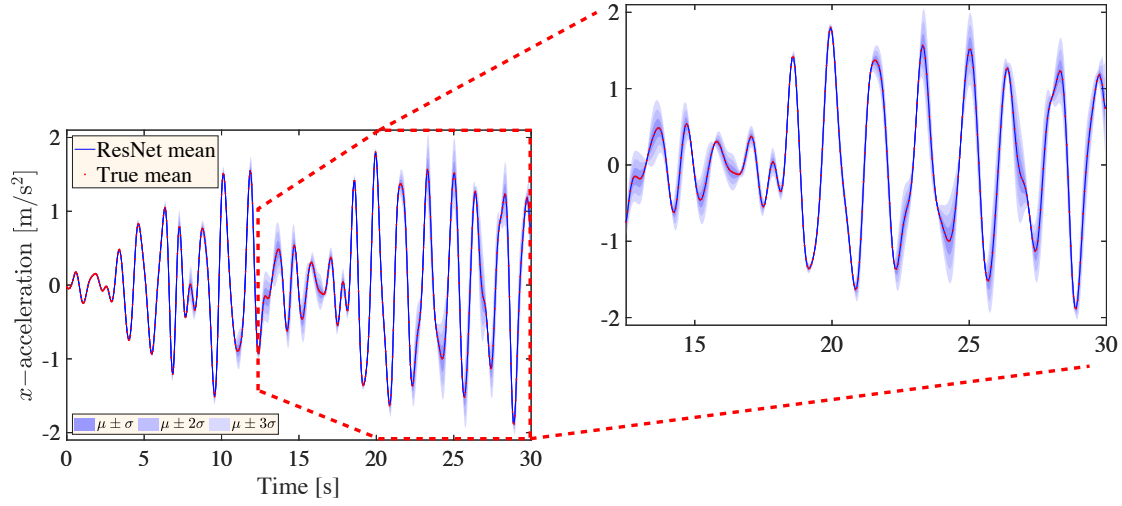
## A Adam Algorithm [60]

In the Adam algorithm, historical gradient information is used to retard the descent along large gradients [60, 61]. This information is stored in  $\hat{\mathbf{m}}$  and  $\hat{\mathbf{v}}$  as

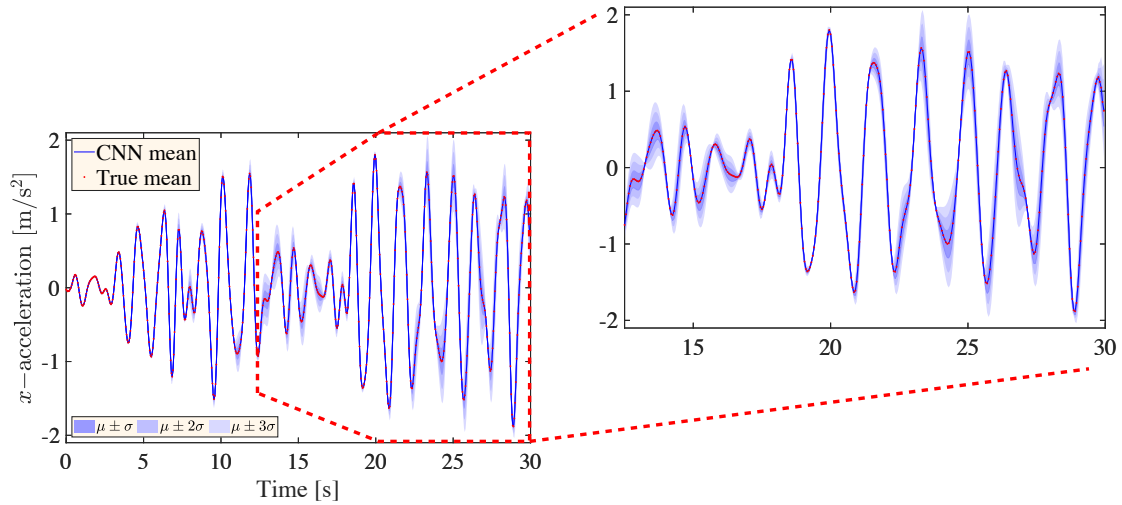
$$\begin{aligned} \mathbf{m}_k &= b_m \mathbf{m}_{k-1} + (1 - b_m) \frac{\partial J}{\partial \boldsymbol{\theta}_k}; & \hat{\mathbf{m}}_k &= \frac{\mathbf{m}^{(k)}}{1 - b_m^k}; \\ \mathbf{v}_k &= b_v \mathbf{v}_{k-1} + (1 - b_v) \left[ \frac{\partial J}{\partial \boldsymbol{\theta}_k} \right]^2; & \hat{\mathbf{v}}_k &= \frac{\mathbf{v}^{(k)}}{1 - b_v^k}, \end{aligned} \quad (28)$$



(a) Prediction of mean and standard deviation of the roof acceleration in  $x$ -direction using FNN

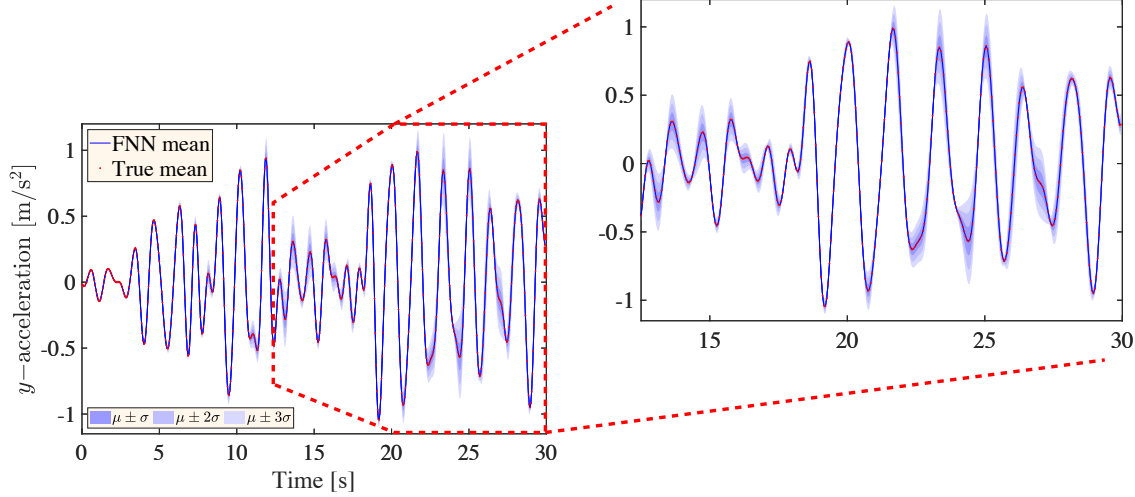


(b) Prediction of mean and standard deviation of the roof acceleration in  $x$ -direction using ResNet

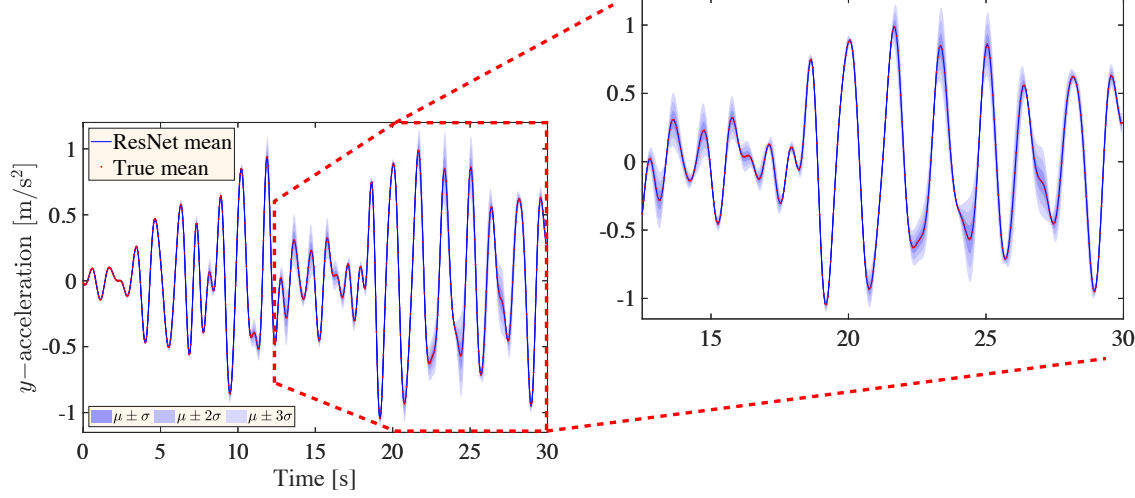


(c) Prediction of mean and standard deviation of the roof acceleration in  $x$ -direction using CNN

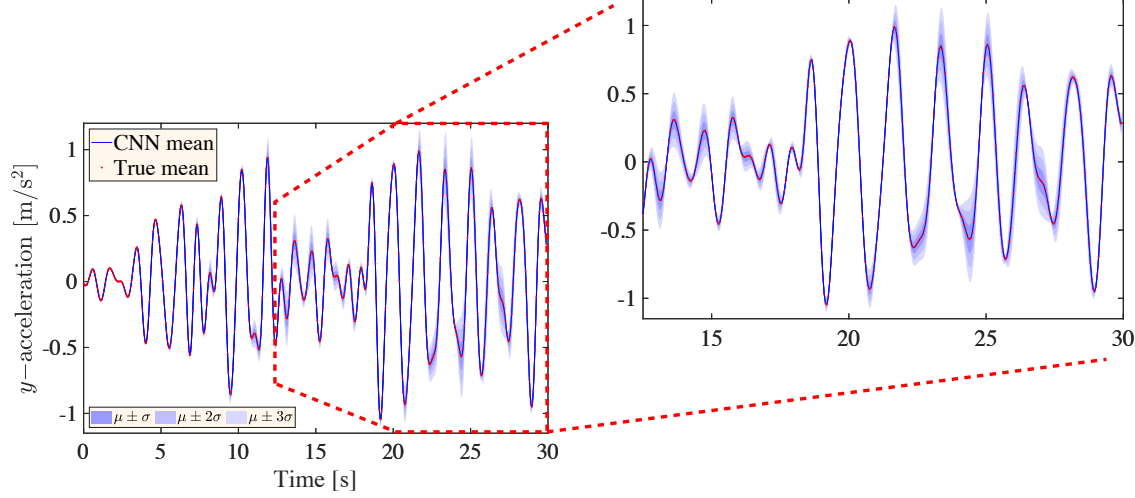
Figure 19: Prediction of the mean and standard deviations of the  $x$ -direction acceleration at the center of the roof from three different neural network architectures using  $10^5$  realizations of the uncertainty in Example III with response in  $[12.5, 30]$  s zoomed in. The mean responses from the neural networks are compared with mean estimated from solving (19) for  $10^5$  realizations of the uncertainty. The shaded regions show combinations of mean  $\mu$  and standard deviation  $\sigma$  of the response.



(a) Prediction of mean and standard deviation of the roof acceleration in  $y$ -direction using FNN



(b) Prediction of mean and standard deviation of the roof acceleration in  $y$ -direction using ResNet



(c) Prediction of mean and standard deviation of the roof acceleration in  $y$ -direction using CNN

Figure 20: Prediction of the mean and standard deviations of the  $y$ -direction acceleration at the center of the roof from three different neural network architectures using  $10^5$  realizations of the uncertainty in Example III with response in  $[12.5, 30]$  s zoomed in. The mean responses from the neural networks are compared with mean estimated from solving (19) for  $10^5$  realizations of the uncertainty. The shaded regions show combinations of mean  $\mu$  and standard deviation  $\sigma$  of the response.

where  $\left[\frac{\partial J}{\partial \theta_k}\right]^2$  is performed element-wise; and  $b_m$  and  $b_v$  are parameters of the Adam algorithm with default values 0.9 and 0.999, respectively. The gradient descent step is applied next as follows

$$\theta_{k+1} = \theta_k - \eta \frac{\hat{\mathbf{m}}_k}{\sqrt{\hat{\mathbf{v}}_k + \epsilon}}, \quad (29)$$

where the above update is performed element-wise and  $\epsilon$  is a very small number to avoid division by zero. We use this algorithm to train the neural networks in this paper. An illustration of the steps of this algorithm is shown in Algorithm 1.

---

**Algorithm 1** *Adam* [60]

---

**Network:**  $\mathcal{M}_{\text{NN}}(\cdot; \theta_0)$

**Given:**  $\eta, b_m, b_v$ , and  $\epsilon$ .

**procedure** ADAM

Initialize  $\theta_1 = \theta_0$ .

Initialize  $\mathbf{m}_0 = \mathbf{0}$ .

Initialize  $\mathbf{v}_0 = \mathbf{0}$ .

**for**  $k = 1, 2, \dots, N_{\text{max}}$  **do**

  Compute  $\frac{\partial J}{\partial \theta_k}$ .

  Set  $\mathbf{m}_k \leftarrow b_m \mathbf{m}_{k-1} + (1 - b_m) \frac{\partial J}{\partial \theta_k}$ .

  Set  $\mathbf{v}_k \leftarrow b_v \mathbf{v}_{k-1} + (1 - b_v) \left[\frac{\partial J}{\partial \theta_k}\right]^2$  (element-wise).

  Set  $\hat{\mathbf{m}}_k \leftarrow \mathbf{m}_k / (1 - b_m^k)$ .

  Set  $\hat{\mathbf{v}}_k \leftarrow \mathbf{v}_k / (1 - b_v^k)$ .

  Set  $\theta_{k+1} \leftarrow \theta_k - \eta \frac{\hat{\mathbf{m}}_k}{\sqrt{\hat{\mathbf{v}}_k + \epsilon}}$  (element-wise).

**end for**

**end procedure**

**Trained network:**  $\mathcal{M}_{\text{NN}}(\cdot; \theta_{N_{\text{max}}})$ .

---

## References

- [1] Timothy Hasselman. Quantification of uncertainty in structural dynamic models. *Journal of Aerospace Engineering*, 14(4):158–165, 2001.
- [2] Kurt Maute and Chris L Pettit. Uncertainty quantification and design under uncertainty of aerospace systems. *Structure and Infrastructure Engineering*, 2(3-4):159–159, 2006.
- [3] William M Bulleit. Uncertainty in structural engineering. *Practice Periodical on Structural Design and Construction*, 13(1):24–30, 2008.
- [4] Roger G Ghanem and Pol D Spanos. *Stochastic finite elements: a spectral approach*. Courier Corporation, 2003.
- [5] Dongbin Xiu and George Em Karniadakis. The Wiener–Askey polynomial chaos for stochastic differential equations. *SIAM journal on scientific computing*, 24(2):619–644, 2002.
- [6] Ivo Babuška, Fabio Nobile, and Raul Tempone. A stochastic collocation method for elliptic partial differential equations with random input data. *SIAM Journal on Numerical Analysis*, 45(3):1005–1034, 2007.
- [7] Fabio Nobile, Raúl Tempone, and Clayton G Webster. A sparse grid stochastic collocation method for partial differential equations with random input data. *SIAM Journal on Numerical Analysis*, 46(5):2309–2345, 2008.
- [8] Christopher KI Williams and Carl Edward Rasmussen. *Gaussian processes for machine learning*. MIT press Cambridge, MA, 2006.
- [9] Alexander IJ Forrester, András Sóbester, and Andy J Keane. Multi-fidelity optimization via surrogate modelling. *Proceedings of the royal society a: mathematical, physical and engineering sciences*, 463(2088):3251–3269, 2007.
- [10] VJ Romero, LP Swiler, and AA Giunta. Construction of response surfaces based on progressive-lattice-sampling experimental designs with application to uncertainty propagation. *Structural Safety*, 26(2):201–219, 2004.
- [11] AA Giunta, JM McFarland, LP Swiler, and MS Eldred. The promise and peril of uncertainty quantification using response surface approximations. *Structures and Infrastructure Engineering*, 2(3-4):175–189, 2006.

- [12] Michael D McKay, Richard J Beckman, and William J Conover. A comparison of three methods for selecting values of input variables in the analysis of output from a computer code. *Technometrics*, 42(1):55–61, 2000.
- [13] Sheldon M Ross. *Simulation*. Academic Press, 5th edition, 2013.
- [14] Mahmoud Kamalzare, Erik A Johnson, and Steven F Wojtkiewicz. Efficient optimal design of passive structural control applied to isolator design. *Smart Structures and Systems*, 15(3):847–862, 2015.
- [15] Subhayan De, Erik A Johnson, and Steven F Wojtkiewicz. Fast Bayesian model selection with application to large locally-nonlinear dynamic systems. In *6th International Conference on Advances in Experimental Structural Engineering, 11th International Workshop on Advanced Smart Materials and Smart Structures Technology*, 2015.
- [16] Subhayan De, Erik A Johnson, Steven F Wojtkiewicz, and Patrick T Brewick. Computationally efficient Bayesian model selection for locally nonlinear structural dynamic systems. *Journal of Engineering Mechanics*, 144(5):04018022, 2018.
- [17] Subhayan De, Steven F Wojtkiewicz, and Erik A Johnson. Efficient optimal design and design-under-uncertainty of passive control devices with application to a cable-stayed bridge. *Structural Control and Health Monitoring*, 24(2):e1846, 2017.
- [18] Aldo A Ferri. Modeling and analysis of nonlinear sleeve joints of large space structures. *Journal of Spacecraft and Rockets*, 25(5):354–360, 1988.
- [19] Mary Bowden and John Dugundji. Joint damping and nonlinearity in dynamics of space structures. *AIAA Journal*, 28(4):740–749, 1990.
- [20] Malte Krack, Loic Salles, and Fabrice Thouverez. Vibration prediction of bladed disks coupled by friction joints. *Archives of Computational Methods in Engineering*, 24(3):589–636, 2017.
- [21] Ren Ying. *The analysis and identification of friction joint parameters in the dynamic response of structures*. PhD thesis, 1992.
- [22] Yongsik Lee and ZC Feng. Dynamic responses to sinusoidal excitations of beams with frictional joints. *Communications in Nonlinear Science and Numerical Simulation*, 9(6):571–581, 2004.
- [23] Olivier Poudou. *Modeling and analysis of the dynamics of dry-friction-damped structural systems*. PhD thesis, 2007.
- [24] Gaurav, SF Wojtkiewicz, and EA Johnson. Efficient uncertainty quantification of dynamical systems with local nonlinearities and uncertainties. *Probabilistic Engineering Mechanics*, 26(4):561–569, 2011.
- [25] Subhayan De, Steven F Wojtkiewicz, and Erik A Johnson. Efficient optimal design-under-uncertainty of passive structural control devices. In *Proceedings of the 12th International Conference on Applications of Statistics and Probability in Civil Engineering (ICASP12)*, 2015.
- [26] Subhayan De, Erik A Johnson, Steven F Wojtkiewicz, and Patrick T Brewick. Efficient Bayesian model selection for identifying locally nonlinear systems incorporating dynamic measurements. In F.-K. Chang and F. Kopsaftopoulos, editors, *Structural Health Monitoring 2015: System reliability for verification and implementation*, volume 2, page 2318–2325. DEStech Publications, Lancaster, PA, 2015.
- [27] Paszke Adam, Gross Sam, Chintala Soumith, Chanan Gregory, Yang Edward, D Zachary, Lin Zeming, Desmaison Alban, Antiga Luca, and Lerer Adam. Automatic differentiation in PyTorch. In *Proceedings of Neural Information Processing Systems*, 2017.
- [28] Martín Abadi, Paul Barham, Jianmin Chen, Zhifeng Chen, Andy Davis, Jeffrey Dean, Matthieu Devin, Sanjay Ghemawat, Geoffrey Irving, Michael Isard, et al. Tensorflow: A system for large-scale machine learning. In *12th USENIX symposium on operating systems design and implementation (OSDI 16)*, pages 265–283, 2016.
- [29] Nathan Baker, Frank Alexander, Timo Bremer, Aric Hagberg, Yannis Kevrekidis, Habib Najm, Manish Parashar, Abani Patra, James Sethian, Stefan Wild, Karen Willcox, and Steven Lee. Workshop report on basic research needs for scientific machine learning: Core technologies for artificial intelligence. Technical report, USDOE Office of Science (SC), Washington, DC (United States), 2019.
- [30] Maziar Raissi, Paris Perdikaris, and George Em Karniadakis. Physics informed deep learning (part I): Data-driven solutions of nonlinear partial differential equations. *arXiv preprint arXiv:1711.10561*, 2017.
- [31] Maziar Raissi and George Em Karniadakis. Hidden physics models: Machine learning of nonlinear partial differential equations. *Journal of Computational Physics*, 357:125–141, 2018.
- [32] Maziar Raissi. Deep hidden physics models: Deep learning of nonlinear partial differential equations. *The Journal of Machine Learning Research*, 19(1):932–955, 2018.



- [33] Maziar Raissi, Paris Perdikaris, and George E Karniadakis. Physics-informed neural networks: A deep learning framework for solving forward and inverse problems involving nonlinear partial differential equations. *Journal of Computational Physics*, 378:686–707, 2019.
- [34] Lu Lu, Xuhui Meng, Zhiping Mao, and George E Karniadakis. DeepXDE: A deep learning library for solving differential equations. *arXiv preprint arXiv:1907.04502*, 2019.
- [35] Ryan King, Oliver Hennigh, Arvind Mohan, and Michael Chertkov. From deep to physics-informed learning of turbulence: Diagnostics. *arXiv preprint arXiv:1810.07785*, 2018.
- [36] Ian Goodfellow. NIPS 2016 tutorial: Generative adversarial networks. *arXiv preprint arXiv:1701.00160*, 2016.
- [37] Karen Stengel, Andrew Glaws, and Ryan King. Physics-informed super resolution of climatological wind and solar resource data. *AGUFM*, 2019:A43E–04, 2019.
- [38] Jan S Hesthaven and Stefano Ubbiali. Non-intrusive reduced order modeling of nonlinear problems using neural networks. *Journal of Computational Physics*, 363:55–78, 2018.
- [39] Qian Wang, Jan S Hesthaven, and Deep Ray. Non-intrusive reduced order modeling of unsteady flows using artificial neural networks with application to a combustion problem. *Journal of Computational Physics*, 384:289–307, 2019.
- [40] Jonathan R Holland, James D Baeder, and Karthik Duraisamy. Towards integrated field inversion and machine learning with embedded neural networks for RANS modeling. In *AIAA Scitech 2019 Forum*, page 1884, 2019.
- [41] Saakaar Bhatnagar, Yaser Afshar, Shaowu Pan, Karthik Duraisamy, and Shailendra Kaushik. Prediction of aerodynamic flow fields using convolutional neural networks. *Computational Mechanics*, 64(2):525–545, 2019.
- [42] Jian-Xun Wang, Junji Huang, Lian Duan, and Heng Xiao. Prediction of reynolds stresses in high-mach-number turbulent boundary layers using physics-informed machine learning. *Theoretical and Computational Fluid Dynamics*, 33(1):1–19, 2019.
- [43] Ruiyang Zhang, Yang Liu, and Hao Sun. Physics-guided convolutional neural network (PhyCNN) for data-driven seismic response modeling. *arXiv preprint arXiv:1909.08118*, 2019.
- [44] Ruiyang Zhang, Zhao Chen, Su Chen, Jingwei Zheng, Oral Büyüköztürk, and Hao Sun. Deep long short-term memory networks for nonlinear structural seismic response prediction. *Computers & Structures*, 220:55–68, 2019.
- [45] Subhayan De, Jolene Britton, Matthew Reynolds, Ryan Skinner, Kenneth Jansen, and Alireza Doostan. On transfer learning of neural networks using bi-fidelity data for uncertainty propagation. *arXiv preprint arXiv:2002.04495*, 2020.
- [46] Xuhui Meng and George Em Karniadakis. A composite neural network that learns from multi-fidelity data: Application to function approximation and inverse PDE problems. *Journal of Computational Physics*, 401:109020, 2020.
- [47] Mohammad Motamed. A multi-fidelity neural network surrogate sampling method for uncertainty quantification. *arXiv preprint arXiv:1909.01859*, 2019.
- [48] Souvik Chakraborty. Transfer learning based multi-fidelity physics informed deep neural network. *arXiv preprint arXiv:2005.10614*, 2020.
- [49] Dongkun Zhang, Lu Lu, Ling Guo, and George Em Karniadakis. Quantifying total uncertainty in physics-informed neural networks for solving forward and inverse stochastic problems. *Journal of Computational Physics*, 397:108850, 2019.
- [50] Yarin Gal and Zoubin Ghahramani. Dropout as a Bayesian approximation: Representing model uncertainty in deep learning. In *international conference on machine learning*, pages 1050–1059, 2016.
- [51] Geoffrey E Hinton, Nitish Srivastava, Alex Krizhevsky, Ilya Sutskever, and Ruslan R Salakhutdinov. Improving neural networks by preventing co-adaptation of feature detectors. *arXiv preprint arXiv:1207.0580*, 2012.
- [52] Xihaier Luo and Ahsan Kareem. Deep convolutional neural networks for uncertainty propagation in random fields. *Computer-Aided Civil and Infrastructure Engineering*, 34(12):1043–1054, 2019.
- [53] Karthik Duraisamy, Gianluca Iaccarino, and Heng Xiao. Turbulence modeling in the age of data. *Annual Review of Fluid Mechanics*, 51:357–377, 2019.
- [54] Souvik Chakraborty. Simulation free reliability analysis: A physics-informed deep learning based approach. *arXiv preprint arXiv:2005.01302*, 2020.
- [55] John Hammersley. *Monte Carlo methods*. Springer Science & Business Media, 2013.

- [56] Bruno Sudret, Stefano Marelli, and Joe Wiart. Surrogate models for uncertainty quantification: An overview. In *2017 11th European Conference on Antennas and Propagation (EUCAP)*, pages 793–797. IEEE, 2017.
- [57] Ian Goodfellow, Yoshua Bengio, and Aaron Courville. *Deep learning*. MIT press, 2016.
- [58] Kaiming He, Xiangyu Zhang, Shaoqing Ren, and Jian Sun. Deep residual learning for image recognition. In *Proceedings of the IEEE Conference on Computer Vision and Pattern Recognition*, pages 770–778, 2016.
- [59] Catherine F Higham and Desmond J Higham. Deep learning: An introduction for applied mathematicians. *arXiv preprint arXiv:1801.05894*, 2018.
- [60] Diederik P Kingma and Jimmy Ba. Adam: A method for stochastic optimization. *arXiv preprint arXiv:1412.6980*, 2014.
- [61] Subhayan De, Jerrad Hampton, Kurt Maute, and Alireza Doostan. Topology optimization under uncertainty using a stochastic gradient-based approach. *arXiv preprint arXiv:1902.04562*, 2019.
- [62] Subhayan De, Kurt Maute, and Alireza Doostan. Bi-fidelity stochastic gradient descent for structural optimization under uncertainty. *arXiv preprint arXiv:1911.10420*, 2019.
- [63] George Cybenko. Approximation by superpositions of a sigmoidal function. *Mathematics of Control, Signals and Systems*, 2(4):303–314, 1989.
- [64] Kurt Hornik, Maxwell Stinchcombe, Halbert White, et al. Multilayer feedforward networks are universal approximators. *Neural Networks*, 2(5):359–366, 1989.
- [65] Kurt Hornik, Maxwell Stinchcombe, and Halbert White. Universal approximation of an unknown mapping and its derivatives using multilayer feedforward networks. *Neural Networks*, 3(5):551–560, 1990.
- [66] JC Ramallo, EA Johnson, and BF Spencer Jr. ‘smart’ base isolation systems. *Journal of Engineering Mechanics*, 128(10):1088–1099, 2002.
- [67] YK Lin and Yan Yong. Evolutionary Kanai-Tajimi earthquake models. *Journal of Engineering Mechanics*, 113(8):1119–1137, 1987.
- [68] Yoshua Bengio. Practical recommendations for gradient-based training of deep architectures. In *Neural networks: Tricks of the trade*, pages 437–478. Springer, 2012.
- [69] Yi-Kwei Wen. Method for random vibration of hysteretic systems. *Journal of the Engineering Mechanics Division*, 102(2):249–263, 1976.
- [70] F Ma, H Zhang, A Bockstedte, Greg C Foliente, and P Paevere. Parameter analysis of the differential model of hysteresis. *J. Appl. Mech.*, 71(3):342–349, 2004.
- [71] Steven F Wojtkiewicz and Erik A Johnson. Efficient sensitivity analysis of structures with local modifications. I: time domain responses. *Journal of Engineering Mechanics*, 140(9):04014067, 2014.
- [72] JD Holmes. Along wind response of lattice towers—III. Effective load distributions. *Engineering Structures*, 18(7):489–494, 1996.